Popular Summary

Introduction to AIRS and CrIS

Joel Susskind

"Introduction to AIRS and CrIS" is a chapter in a book dealing with various aspects of remote sensing. AIRS and CrIS are both high spectral resolution IR sounding instruments, which were recently launched (AIRS) or will soon be launched (CrIS). The chapter explains the general principles of infra-red remote sensing, and explains the significance and information content of high spectral resolution IR measurements. The chapter shows results obtained using AIRS observations, and explains why similar quality results should be obtainable from CrIS data.

Introduction to AIRS and CrIS

DR. JOEL SUSSKIND

Laboratory for Atmospheres

NASA Goddard Space Flight Center

Greenbelt, MD 20771

e mail: Joel.Susskind-1@nasa.gov
telephone: 301-286-7210
fax: 301-286-2323

Overview

AIRS/AMSU/HSB is a state of the art advanced infra-red microwave sounding system that was launched on the EOS Aqua platform in a 1:30 AM/PM sun synchronous orbit on May 5, 2002. An overview of the AIRS instrument and the objectives for AIRS/AMSU/HSB is a given in Pagano et al. (2003). The sounding goals of AIRS are to produce 1 km tropospheric layer mean temperatures with an rms error of 1K, and 1 km tropospheric layer precipitable water with an rms error of 20%, in cases with up to 80% effective cloud cover. Aside from being part of a climate mission, one of the objectives of AIRS is to provide sounding information of sufficient accuracy such that when assimilated into a general circulation model, significant improvement in forecast skill would arise. The pre-launch algorithm to produce level 2 products (geophysical parameters) using AIRS/AMSU/HSB data, and expected results based on simulation studies, are given in Susskind et al. (2003). The results of that simulation indicate that the sounding goals of AIRS/AMSU/HSB should be achievable.

CrIS, like AIRS, is an advanced IR sounder that will fly on the NPP mission scheduled for launch in 2006, as well as on NPOESS, the future low earth orbiting operational satellite series. CrIS will be accompanied by ATMS, a microwave sounder with characteristics similar to those of AMSU A/HSB. CrIS/ATMS is expected to produce products of similar accuracy as can be obtained from AIRS/AMSU/HSB.

Both AIRS and CrIS are high spectral resolution ($\nu/\Delta\nu \approx 1000$) IR sounders with many channels covering the spectral range 650 cm^{-1} – 2700 cm^{-1}. Most of these channels are opaque, due to atmospheric absorption. Opaque channels are referred to as sounding channels, while channels in which the atmosphere has little absorption are called window channels. Observations in the sounding channels are sensitive to atmospheric temperature and constituent profiles and can be used to determine these parameters. The spatial resolution of AIRS and CrIS is on the order of 15 km at nadir and is coarse compared to that of imagers such as MODIS and VIIRS, which is on the order of 1 km. Accurate soundings can be done in the presence of broken clouds with a coupled IR/microwave sounding

system, and while very high spatial resolution is desirable, it is not critical for the production of accurate soundings. On the other hand, higher spatial resolution is required to the extent that sounding products at higher spatial resolution are desired. Both AIRS and CrIS contain a 3x3 array of observations within a single AMSU A like footprint (called field of regard – FOR), and a single sounding will be produced within a given FOR, with a spatial resolution of 50 km at nadir (growing to roughly 70 km by 150 km at the largest satellite zenith angle).

High spectral resolution observations in the infra-red are desirable for a number of reasons. Both AIRS and CrIS contiguously cover the spectral interval 650 cm^{-1} to 2650 cm^{-1}, with some planned spectral gaps. AIRS has 2378 channels with a resolving power $\nu/\Delta\nu \approx 1200$ where $\Delta\nu$ is the spectral half-width of a channel at frequency ν, and CrIS has 1286 channels with $\nu/\Delta\nu \approx 650$. Both AIRS and CrIS are sampled with a frequency spacing of roughly $\Delta\nu/2$. Having a large number of channels with high spectral resolution allows for isolation of absorption features primarily due to a single gaseous absorption line, or in between absorption lines. This allows for selectivity of channels to be used when analyzing the data. The best channels are primarily sensitive to absorption by a single species. For temperature sounding, it is optimal to use channels in which absorption is primarily due to CO_2 and N_2O, whose concentrations are very close to constant in space and time. Absorption features due primarily to H_2O, O_3, CH_4, and CO are used to determine the concentration profiles of these gases, which vary significantly in space and time. Depending on the purpose, the best channels for sounding purposes are usually either between lines or on line centers.

The fact that adequate information about the surface and atmosphere can be obtained from analysis of only a subset of channels demonstrates that there is much more independent spectral information about the earth than there are degrees of freedom in the geophysical space of surface and atmospheric parameters. As a consequence of this, the effective noise of the spectrum is actually lower than that of the individual channels as observations in channels with redundant geophysical information can be used together so as to reduce the effective observational noise.

The AIRS science team is currently deriving a number of geophysical parameters from analysis of AIRS/AMSU sounding data. The primary products are atmospheric temperature profiles from the surface to 0.1 mb, water vapor profile for the surface to 100 mb, and ozone profile from the surface to 0.1 mb; land/ocean surface skin temperature and IR and microwave spectral emissivity; AIRS clear column radiances, which are the radiances that would have been seen if the atmosphere had no clouds; cloud top pressure and effective fractional cloud cover for up to two cloud types; and Outgoing Longwave Radiation (OLR) and clear sky OLR (the Longwave radiation which would have gone to space if no clouds were present (Mehta and Susskind, 1999)). Atmospheric profiles of CO and CH_4, as well as total integrated atmospheric CO_2 burden are being derived in a research mode.

Figure 1 shows a sample AIRS spectrum. Channels used for different purposes are indicated as stars, with different colors depicting the geophysical parameter

derived from that channel. AIRS has a number of mini spectral gaps, which are portrayed as gaps in the spectra shown. There is also a large spectral gap between 1614 cm^{-1} and 2181cm^{-1}. Very little additional information about the earth's surface and atmosphere is contained by channels in these spectral gaps. The meaning of the features shown in the AIRS spectrum will be discussed in detail later in this chapter.

Both AIRS and CrIS are accompanied by a microwave sounding instrument. IR and microwave observations are very complementary and the strengths of a combined system are greater than the sum of the strengths of the individual components. As shown in the next section, high resolution IR observations produce higher vertical resolution, and hence better accuracy, of mid-lower tropospheric temperature profile than the microwave observations. In addition, high spectral resolution IR observations provide the best information about surface skin temperature and constituent profiles. A major complication with regard to IR observations is that most IR channels are affected by scattering due to clouds in the FOR. Therefore, cloud effects must be well accounted for in order to take full advantage of the inherent capabilities of high spectral resolution IR observations.

Microwave observations are not appreciably affected by scattering due to (non-precipitating) clouds. Combined microwave and IR observations can be used to accurately account for the effects of clouds on the IR observations and produce accurate soundings in up to 80% partial cloud cover in the FOR (Susskind et al., 2003). Microwave soundings can also be used to produce temperature-moisture profiles under up to overcast conditions with non-precipitating clouds. The inherent accuracy of these is poorer than what would have been obtained if the high spectral resolution IR observations cloud have been used effectively however.

The Radiative Transfer Equation

The monochromatic radiance going to space at frequency ν, in the IR and microwave spectral regions, under clear sky conditions is given in equation 1.

$$R_{\nu,clr} = \varepsilon_\nu B_\nu(T_s)\tau_\nu(p_s) + \int B_\nu[T(p)]\left(\frac{d\tau_\nu}{d\ell np}\right)d\ell np + \rho_\nu H_\nu \tau'_\nu(p_s) \qquad (1)$$

$$+(1-\varepsilon_\nu)R_\nu \downarrow \tau_\nu(p_s)$$

The first term in equation 1 represents radiation emitted by the surface transmitted through the atmosphere in the direction of the satellite, and the second term represents radiation emitted by the atmosphere transmitted to the satellite. These are the two main contributions to the observed radiances. The third and fourth terms represent downwelling radiation, reflected by the surface and transmitted to the satellite, coming either from the sun (third term) or the atmosphere (fourth term). The third term is significant only during the day and primarily at frequencies greater than 2400 cm^{-1}. The fourth term is generally very small and will not be discussed here.

The most important terms in equation 1 are the Planck Black Body function $B_\nu(T)$, where ν is the frequency and T is the temperature; $\tau_\nu(p)$, the atmospheric transmittance at frequency ν from pressure p to the satellite; and $\frac{d\tau_\nu}{d\ell np}$, the derivative of $\tau(p)$, also referred to as the weighting function W(p). Two surface parameters found in equation 1 are the spectral surface emissivity, ε_ν, and the surface spectral bidirectional reflectance of solar radiation, ρ_ν. In addition, the surface skin temperature T_s is a dominant factor affecting the first term.

The atmospheric transmittance $\tau_\nu(p)$ is given by

$$\tau_\nu(p) = e^{-\int_0^p \sum_\ell k_{\nu\ell}(p)\, c_\ell(p)\, dp} \qquad (2)$$

where ℓ refers to different absorbing species, $k_{\nu\ell}(p)$ is the absorption coefficient for species ℓ at frequency ν, and $c_\ell(p)$ is the fraction of air (mixing ratio) of species ℓ at pressure p.

The radiance at frequency ν reaching the satellite hence depends on the surface parameters $\varepsilon_\nu, \rho_\nu$, and T_s; the atmospheric temperature profile T(p); and the constituent profiles through their effects on $\tau(p)$ and $\frac{d\tau}{d\ell np}$. $\tau(p)$ also depends on the temperature profile as $k_{\nu\ell}$ is temperature dependent. $\tau_\nu(p)$ varies from 1, at the satellite, to $\tau_\nu(p_s)$ at the surface, where p_s is the surface pressure. At frequencies in which the absorption coefficients $k_{\nu\ell}$ are very small, $\tau_\nu(p_s)$ is close to 1.0. These frequencies are referred to as windows, and the first (and third) terms of equation 1 dominate the observed radiances. At frequencies in which values of $k_{\nu\ell}$ are large, $\tau(p_s)$ can be extremely small. At these frequencies, radiation emitted or reflected by the surface is not transmitted back to satellite, and only the second term contributes to the observed radiances.

In the vicinity of opaque channels, the spectral shape of the radiance spectrum R_ν depends on the weighting function $W_\nu(p)$. $B_\nu[T(p)]$ in equation 2 is weighted in the integral by $\frac{d\tau_\nu}{d\ell np}$. The integral of this weighting, $\frac{d\tau}{d\ell np} d\ell np$, is equal to the integral of $d\tau$ which is $1 - \tau(p_s)$. Hence term 1 contributes $\tau(p_s)$ to the total radiance and term 2 contributes $1 - \tau(p_s)$ to the total radiance. For opaque channels, term 2 is the sole contributor. Moreover, the contribution to the integral is significant only over the atmospheric pressure range in which $\tau(p)$ is changing. High in the atmosphere (how high depends on k_ν), $\tau_\nu(p)$ is close to 1.0 and $d\tau / d\ell np$ is close to zero. Near the surface (how near depends on k), $\tau_\nu(p)$ is close to 0.0 and $d\tau / d\ell np$ is close to 0. The pressure range in which $\tau_\nu(p)$ changes from near 1 to near 0 is the range which contributes to the radiance, and

hence the range in which T(p) and $c_\ell(p)$ contribute to the radiance in that channel.

A simplified expression for $W_\nu(p)$ is obtained for the case in which only one gas, ℓ, is absorbing, and c_ℓ and $k_{\nu\ell}$ are constant in pressure. Under these conditions,

$$\tau_\nu(p) = e^{-k_\nu cp} \qquad (3)$$

and

$$W_\nu(p) = k_\nu cp e^{-k_\nu cp} = xe^{-x} .$$

The maximum value of $W_\nu(p)$ is then given by 0.37 when x=1. The pressure $p_{\nu\,max}$ at which the weighting function is maximum is given by

$$p_{\nu\,max} = \frac{1}{k_\nu c} .$$

Thus, for a given c, $p_{\nu\,max}$ is lower (higher in the atmosphere) for large values of k_ν and higher for lower values of k_ν. The radiance will depend on the Planck function of temperature averaged over the vicinity of $p_{\nu\,max}$.

A weighting function of the form xe^{-x} is quite broad in terms of ℓnp. Therefore, the radiance for such a channel corresponds to the temperature distribution over a wide range of the atmosphere. For the purpose of inferring temperature profile from the observed radiance spectrum, it is better to use observations in which the appropriate weighting functions are narrow (Kaplan et al., 1976). The weighting function will be narrower (that is τ drops from 1 to 0 faster) if k increases with p, as occurs at frequencies in the wing of a Lorentz broadened line, or k increases with T and T increases with p. Observations in such frequencies are particularly good for temperature sounding purposes. Observations on channel line centers are particularly poor to use because at these frequencies, k decreases with increasing p and the weighting functions are broader than xe^{-x}. The weighting function also will be sharper if c increases with p (as it does for tropospheric water vapor). Observations at frequencies for which water vapor is the main absorber are not optimal for temperature sounding purposes because while the weighting functions are sharp, one does not know their peaks as they depend on c, which is highly variable for tropospheric water vapor in space and time.

Instruments do not measure monochromatic radiances however. Instruments are characterized by a set of channels, i, with characteristic channel spectral response functions, $f_i(\nu)$. The channel radiance R_i measured by channel i is given by

$$R_i = \int R_\nu f_i(\nu) d\nu / \int f_i(\nu) d\nu \qquad (4)$$

The spectral resolution $\Delta\nu$ alluded to earlier for AIRS and CrIS refers to the full width at half-maximum (FWHM) of $f_i(\nu)$. If $\Delta\nu_i$ is narrow, as it is for AIRS and CrIS channels, then, to a very good approximation,

$$R_i \approx \varepsilon_i B_i(T_s)\tau_i(p_s) + \int B_i[T(p)]W_i(p)d\ell np + \rho_i H_i \tau_i'(p_s) + (1-\varepsilon_i)R_i\downarrow\tau_i p_s \quad (5)$$

where every term with subscript i is the channel average of the analogous term with subscript ν, as done in equation 4. To first order, the spectral response function for AIRS channel i is a Gaussian function centered at ν_i with FWHM = $\nu/1200$.

Figure 1 showed the observations for the AIRS channels in terms of brightness temperatures. The brightness temperature Θ_i for channel i, with a radiance R_i, is defined as

$$\Theta_i = B_i^{-1}(R_i), \quad (6)$$

that is, Θ_i is the temperature at frequency ν_i for which the Planck function would be R_i. There is a unique monotonic relationship between R_i and Θ_i.

Under partial cloud cover, the radiance is given by

$$R_i = \left(1 - \sum_j \alpha_j\right) R_{i,clr} + \sum_j \alpha_j R_{i,cldj} \quad (7)$$

where α_j is the fraction of the sky, as seen from the satellite, covered by cloud type j and $R_{i,cldj}$ is the channel i radiance going to the satellite which would be seen if the whole field of view were covered by cloud type j. For cloud clearing purposes, it is not necessary to know or be able to calculate $R_{i,cldj}$. In constructing the simulated radiance shown in Figure 1, clouds were treated as black bodies with a temperature equal to the atmospheric temperature at the cloud top pressure. This scene has only 10% cloud cover and is mostly clear.

Window regions exist between roughly 760 cm^{-1} and 1000 cm^{-1}, 1080 cm^{-1} and 1250 cm^{-1}, and 2440 cm^{-1} and 2670 cm^{-1}. In the first two spectral regions, the brightness temperatures between absorption lines are approximately 294 K. Brightness temperatures at 2600 cm^{-1} are closer to 300 K because of the contribution of solar radiation reflected by the surface to the observed radiances. On the weak line centers in these windows, brightness temperatures are colder, because the satellite sees less of the warmer surface (weighted by $\tau_i(p_s)$), and more of the colder air temperature $\overline{T}(p)$ above the surface (weighted by $(1-\tau_i(p_s))$, where $\overline{T}(p_i)$ is an effective atmospheric temperature averaged over the channel weighting functions. Thus the brightness temperature is the weighted

average of the surface skin temperature and the effective atmospheric temperature. As $\tau_i(p_s)$ goes to zero, the brightness temperature becomes equal to the effective atmospheric temperature, roughly approximated by the temperature at the peak of the channel weighting function.

Figure 2 shows sample weighting functions for selected AIRS-like channels and for the temperature sounding channels of AMSU A. The sharpest temperature weighting functions for AIRS are in the lower troposphere and are in channels in the vicinity of 2390 cm^{-1}. These channels have sharp weighting functions primarily because the absorption coefficient of the absorbing gas, CO_2, increases rapidly with increasing temperature at these frequencies (Kaplan et al., 1976). These channels provide the most important information about lower tropospheric temperature and are a subset of the red temperature sounding channels indicated in Figure 1. Most of the other channels used for temperature sounding are between lines (locally warmer than line centers) in the spectral region 750 cm^{-1} – 700 cm^{-1}, and locally cooler than the line centers between 650 cm^{-1} and 700 cm^{-1}. In this latter area of the spectrum, emission is coming primarily from the stratosphere, in which temperature increases with increasing height. Hence more weakly absorbing channels (between lines) see lower in the atmosphere, which is cooler, than do channels on adjacent line centers. The local maximum in brightness temperature at 667 cm^{-1} (called the CO_2 Q branch) is a very opaque spectral region in which emission comes from as high as 1 mb. Channels 10-12 in Figure 2 give examples of weighting functions in the CO_2 Q branch. Upper tropospheric temperatures (300 mb and lower pressures) can be determined about as well from AMSU A channels 8-15 as they can be determined from AIRS channel observations. CO_2 absorption features are also used to determine total CO_2 column amount. These are shown in dark blue in figure 2, and generally lie on the line centers of CO_2 absorption lines between 710 cm^{-1} and 740 cm^{-1}.

The spectral feature in the vicinity of 1000 cm^{-1} – 1070 cm^{-1} is due primarily to O_3 absorption, and a number of channels, shown in green, are use to determine the O_3 profile. Water vapor absorption is prominent in the spectral region 1300 cm^{-1} – 1600 cm^{-1}. Water vapor is determined using the light blue channels, looking both between lines and on line centers. Water vapor lines are also used in window regions, both on weak water vapor lines as well as between lines. The strong absorption feature at 1306 cm^{-1} is due to methane, as are a number of nearby weaker absorption features. Channels used to determine the methane profile are shown in orange. Absorption by CO occurs near 2200 cm^{-1}, and a number of CO sounding channels are shown in purple.

Results using AIRS/AMSU Data

The results shown below represent the state of products delivered by the AIRS Science Team algorithm as of January 30, 2004. Improvements to the algorithm continue to be made. The AIRS Science Team retrieval algorithm is basically identical to the pre-launch algorithm described in Susskind et al. (2003). The major difference is the addition of terms to account for systematic errors in

computed channel radiances resulting from an imperfect parameterization of the physical processes affecting the radiances, as well as addition of a term in the channel noise covariance matrix expressing residual errors in computed channel radiances after the systematic errors are accounted for. The need for these terms was alluded to in Susskind et al. (2003), in which the simulation study did not account for errors in the parameterization of the radiative transfer physics.

The key steps of the AIRS Science Team algorithm are listed below:

1) Start with an initial state consistent with the AMSU A and HSB radiances (Rosenkranz, 2000); 2) Derive IR clear column radiances $\hat{R}_i^0$ valid for the 3x3 AIRS Fields of View (FOVs) within an AMSU A Field of Regard (FOR) consistent with the observed radiances and the initial state; 3) Obtain an AIRS regression guess (Goldberg et al., 2003) consistent with $\hat{R}_i^0$ using 1504 AIRS channels; 4) Derive $\hat{R}_i^1$ consistent with the AIRS radiances and the regression guess; 5) Derive all surface and atmospheric parameters using $\hat{R}_i^1$ for 415 AIRS channels and all AMSU and HSB radiances; 6) Derive cloud parameters and OLR consistent with the solution and observed R_i; 7) Apply quality control, which rejects a solution if the retrieved cloud fraction is greater than 80% or other tests fail. In the event that a retrieval is rejected, cloud parameters are determined using the initial microwave state and observed AIRS radiances.

Figure 3 shows the number of cases for each retrieved effective fractional cloud, in 0.5% bins, for the whole day September 6, 2002. The effective fractional cloud cover is given by the product of the fraction of the field of view covered by clouds and the cloud emissivity at 11 mm. The average global effective cloudiness was determined to be 41.20%. Also shown is the percent of accepted retrievals as a function of retrieved effective cloud cover. Roughly 90% of the cases with retrieved effective cloud cover 5% were accepted, falling to 35% at 40% effective cloud cover, and to 18% at 80% effective cloud cover. All cases with retrieved effective cloud cover greater than 80% are rejected. The average effective fractional cloudiness for all accepted cases was 24.61%.

Figure 4 shows the RMS difference between retrieved 1 km layer mean temperatures and the collocated ECMWF forecast for all accepted cases as a function of retrieved effective cloud fraction. Results are shown for each of the lowest 8 km of the atmosphere. Agreement degrades with increasing cloud cover, but only very slowly except in the lowest 1 km of the atmosphere. RMS temperature differences from ECMWF at all levels are somewhat larger than the 1 K goal for retrieval accuracy. Part of this difference can be attributed to the fact that the ECMWF forecast is not perfect. It is also possible that the accuracy of the ECMWF forecast may be somewhat poorer with increasing cloud cover. The increase in RMS temperature differences at 0% cloudiness is somewhat misleading because a large percentage of clear cases occurred over Antarctica on this day.

Figures 5a and 5b show RMS differences of temperature and moisture profiles from the "truth" with both simulated and real data. The gray and black curves

reflect all accepted cases, and the pink and red curves are cases identified as clear, for simulated and observed radiances respectively. For temperature, 1 km layer mean differences from the truth are shown, and for water vapor, % differences in total integrated water vapor in 1 km layers are shown. In simulation, the truth is known perfectly, while with real data, the 3 hour ECMWF forecast is taken as a proxy for "truth". For real data, as in simulation, temperature retrievals under cloudy conditions (roughly 47% of all cases are accepted) degrade by only a few tenths of a degree compared to cases identified as clear (roughly 3% of the cases are identified as clear), while water vapor retrievals do not degrade at all. Differences from "truth" are poorer with real data than in simulation. Two major causes of degradation are: 1) perfect physics was assumed in simulation; and 2) the "truth" has errors in real data. The degradation of soundings in the presence of "real clouds", as compared to soundings in clear cases, appears to be similar to that implied by simulation.

Figure 6a shows RMS layer mean temperature differences between accepted retrievals, the ECMWF forecast, and collocated radiosonde reports (± 1 hour, ± 100 km) for September 6, 2002. The number of cases included in each of the layers is indicated at the right of the figure. It is interesting to note that the RMS temperature differences between the retrievals and ECMWF are generally smaller in the vicinity of radiosondes than they were globally (see Figure 5a). This is because the ECMWF forecast is more accurate in the vicinity of radiosondes than it is globally. The 3 hour ECMWF forecast agrees with radiosondes to 1 K between roughly 750 mb and 20 mb. Spatial and temporal sampling differences between ECMWF, retrievals, and radiosondes contribute to some extent to the increased differences between both ECMWF and retrievals as compared to radiosondes beneath 750 mb, as spatial and temporal variability of the atmosphere is greatest near the surface. Retrieval accuracy near radiosondes is somewhat poorer than that of the forecast at all levels, especially in the vicinity of 200 mb. This is most likely due to limitations in the current methodology used to account for systematic errors in the radiative transfer used in the calculations and accounting for residual physics errors in the channel noise covariance matrix. Improvement is expected in this area with further research.

Figure 6b shows analogous results for percent differences in 1 km layer mean precipitable water, for which the sounding goal for AIRS is 20%. With regard to water vapor, it is clear that AIRS retrievals are significantly more accurate than the ECMWF forecast above 700 mb. AIRS differences from radiosondes are greater than the 20% goal. Spatial and temporal sampling differences between AIRS and radiosondes may contribute significantly to the apparent water vapor "errors" as water vapor changes rapidly in space and time.

Figure 7a shows the retrieved effective cloud top pressure and effective cloud fraction for ascending orbits on January 25, 2003. The results are presented in terms of cloud fraction in 5 groups, 0-20%, 20-40%, etc. with darker colors indicating greater cloud cover. These groups are shown in each of 7 colors, indicative of cloud top pressure. The reds and purples indicate the highest clouds, and the yellows and oranges the lowest clouds. Cloud fields are retrieved for all cases in which valid AIRS/AMSU observations exist. Gray means no data was

observed. Figure 7b shows the retrieved 500 mb temperature field. Gray indicates regions where either no valid observations existed or the retrieval was rejected, generally in regions of cloud cover 80-100%. Retrieved temperature profile fields are quite coherent, and show no apparent artifacts due to clouds in the field of view. Figures 7c and 7d show retrieved values of total precipitable water vapor above the surface and above 300 mb. Note the high values of upper tropospheric water vapor to the east of extensive cloud bands attributed to cold fronts.

Figure 8a shows the retrieved 700 mb temperature field for ascending orbits on January 25, 2003. Figure 8b shows the collocated ECMWF 3 hour forecast 700 mb temperature field. These fields appear very similar to each other. Their difference is shown in Figure 8c, in which white shows agreement to ± 0.5K, each shade of red shows AIRS warmer than ECMWF in intervals of 1 K (0.5 – 1.5, 1.5 – 2.5, etc.), and each shade of blue shows AIRS colder then ECMWF in intervals of 1 K. The area weighted global mean difference of the two fields is 0.08 K, and the area weighted standard deviation is 1.13 K. Most areas are white or the first shade of red or blue. The largest differences between the two fields occur in the vicinity of 35°S – 55°S, 100°E – 140°E, and show up as a dipole, with AIRS warmer to the west of 120°E and colder to the east. Figures 8a and 8b show this to be an area of a cold air mass, extending from the polar region to the mid-latitudes. This cold air mass is coherent in both the retrieved and forecasted fields, but is centered further east in the retrieved field compared to the forecast field, corresponding to a phase error in the 3 hour ECMWF forecast. This is precisely the type of information that satellite data can provide (if accurate enough) to help improve forecast skill. Figure 8d shows the difference between the retrieved and forecast 100 mb temperature fields. At the 100 mb level, a corresponding warm front (not shown) exists in both the retrieved and forecast fields in the area discussed above, with an analogous phase error to that found at 700 mb. Consequently, the retrieved 100 mb field is cooler than ECMWF to the west and warmer to the east in the region discussed above. This out of phase relationship of patterns of differences from ECMWF at 700 mb and 100 mb is indicative of phase errors in the ECMWF forecast, as there is no reason for retrieval errors to be out of phase with each other at 700 mb and 100 mb. This out of phase relationship in spatial patterns of differences between retrieved and forecast temperatures at 700 mb and 100 mb is found in numerous places in Figures 8c and 8d and indicates many areas where the satellite data should improve the ECMWF forecast.

Forecast Impact Experiments

The data assimilation system used in the experiments is FVSSI which represents a combination of the NASA Finite Volume General Circulation Model (FVGCM) with the NCEP operational Spectral Statistical Interpolation (SSI) global analysis scheme implemented at lower than the operational horizontal resolution – T62. The basics of the finite-volume dynamical core formulation are given in DAO's Algorithm Theoretical Basis Document (see **http://polar.gsfc.nasa.gov/sci_research/atbd.php**), and the FVGCM has been

shown to produce very accurate weather forecasts when run at high resolution (Lin et al., 2004). The AIRS temperature profiles produced by SRT were presented to the SSI analysis as rawinsonde profiles with observational error specified at 1°K at all vertical levels.

Results are presented for three sets of experiments in which data was assimilated for the period January 1 – January 31, 2003. Five day forecasts were run every two days beginning January 6, 2003 and forecasts every 12 hours were verified against the NCEP analysis, which was taken as "truth". In the first experiment, called "control", all the data used operationally by NCEP was assimilated, but no AIRS data was assimilated. The operational data included all conventional data, TOVS and ATOVS radiances for NOAA-14, 15, and 16, cloud tracked winds, SSM/I total precipitable water and surface wind speed over ocean, QuikScat surface wind speed and direction, and SBUV ozone profiles. In the second and third experiments, called "clear AIRS" and "all AIRS", temperature profiles retrieved from AIRS soundings were assimilated in addition to the data included in the "control" experiment. "Clear ocean" included all accepted temperature retrievals derived from AIRS over ocean and sea ice in cases where the retrieved cloud fraction derived from AIRS was less than or equal to 2%, while the "all ocean" experiment assimilated accepted AIRS temperature soundings over ocean and sea ice for all retrieved cloud fractions.

Figure 9 shows anomaly correction coefficients of forecast sea level pressure verified against the NCEP analysis for both Northern Hemisphere extra-tropics and Southern Hemisphere extra-tropics for both the "control" and "all AIRS" experiments. An anomaly coefficient of 0.6 or greater indicates a skillful forecast. In the Northern Hemisphere, addition of all AIRS soundings resulted in an improvement in average forecast skill of the order of 1 hour or less, but an improvement in average forecast skill in the Southern Hemisphere on the order of 6 hours results from assimilation of AIRS soundings, that is, equivalent forecast skill occurs 6 hours later when AIRS data is used. Assimilation of AIRS soundings only under essentially clear conditions (not shown), resulted in somewhat poorer forecasts than using all AIRS soundings. It should be noted that the Aqua orbit (1:30 ascending) is almost identical to that of NOAA 16 carrying HIRS3, AMSU A and AMSU B, so AIRS/AMSU/HSB soundings are providing additional information to that contained in the AMSU A/AMSU B radiances on NOAA 16 in the same orbit.

Figure 10 shows the RMS position error (km) and magnitude error (hPa) for 5 day forecasts of extra tropical cyclones in the three experiments. It is apparent that addition of AIRS soundings improved RMS forecast skill for both the position and magnitude of extra-tropical cyclones globally, and addition of AIRS soundings in partially cloudy areas further improved forecast skill as compared to use of soundings only in essentially clear conditions.

Several thousand cyclones verifications are included in these statistics. Addition of AIRS data did not improve forecasted cyclone position and intensity for each cyclone. Some were improved substantially however. Figure 11 shows the impact of AIRS data on the 24 hour forecast of position and intensity of tropical storm Beni, which was centered roughly 4° east of New Caledonia on January 31, 2003

with a central pressure of 990 mb (see Figure 11d). The control forecast (Figure 11a) produced a relatively weak cyclone (1007 mb) displaced considerably to the northwest, while the 24 hour forecast using AIRS data (Figure 11b) was much more accurate in both position and intensity (995 mb). It is significant to note that our forecast using AIRS data was more accurate in both position and intensity than the NCEP operational forecast (Figure 11c) in this case, which, even though it used a higher resolution model and analysis system, did not have the benefit of AIRS data. The results shown indicate the potential of AIRS soundings to improve operational forecast skill. We are working with NCEP to arrange an experiment to add AIRS temperature soundings to an otherwise equivalent run on the NCEP computing system to see the extent, if any, that operational forecast skill can be improved upon.

Comparison of CrIS and AIRS

CrIS was designed to be a follow on to AIRS and has generally similar characteristics. AIRS is a multidetector array grating spectrometer and CrIS is an interferometer. These are two hardware approaches toward achieving roughly the same spectral and noise characteristics, and from the theoretical or practical perspectives, the difference in hardware approach poses only second order effects on the data.

The raw data product from an interferometer, the interferogram, is a cosine transform of the incoming radiance. One obtains the channel i radiance R_i by taking the cosine transform of the product of the interferogram $I(\delta)$ with an apodization function , where δ is the optical path difference. The cosine transform has finite limits, since the interferometer has a finite maximum optical-path difference L:

$$R_i = \frac{\int_{\delta=-\infty}^{\infty} A(\delta)\cdot I(\delta)\cdot \cos(2\pi(\nu-\nu_i)\cdot\delta)\cdot d\delta}{\int_{\delta=-\infty}^{\infty} A(\delta)\cdot d\delta} \quad . \tag{8}$$

In the interferogram domain, the unapodized (or boxcar) apodization function is defined as

$$\begin{aligned} A^u(\delta) &= 1 \quad \text{for} |\delta| \le L \\ &= 0 \quad \text{for} |\delta| > L \ . \end{aligned} \tag{9}$$

The channel spectral response funciton, $f_i(\nu)$, is the cosine transform of the apodization function. For an unapodized interferometer, $f_i^u(\nu)$ is equal to

$$f_i^u(\nu) = \frac{\sin(y)}{y} + \frac{\sin(z)}{z} = \sin c(y) + \sin c(z) \tag{10}$$

where $y = 2\pi L \cdot (\nu - \nu_i)$, $z = 2\pi L \cdot (\nu + \nu_i)$, ν_i is the channel center , and ν is the frequency. Typically, the second term in equation 10 is ignored.

The Nyquist sampling theorem states that the optimal sampling of channels is such that the channel spacing is $\delta\nu = 1/(2L)$ in the frequency domain (Brigham, 1988). No additional information is gained by sampling the interferogram at a higher rate (although oversampling is used to reduce out-of-band aliasing). However, information is lost if the interferogram is sampled at a lower rate.

The sinc(y) function is shown as the red curve in Figure 12 for $L = 0.8$ cm^{-1}, the value of L in band 1 of CrIS. The sinc(y) function has large side-lobes that alternate in sign between the zeros of the function spaced at $y = \pm n\pi$. FWHM of the sinc(y) function is equal to

$$FWHM^u = \frac{0.603355}{L} \approx \frac{1.2}{2L} \quad . \tag{11}$$

Only 45% of the area of the unapodized spectral response function comes from the central lobe.

The use of nonlocalized, unapodized radiances can produce complications in the retrieval of geophysical parameters. For multispectral retrievals (e.g. combining microwave and IR readiances) it is convenient, but not necessary, to represent radiances as brightness temperatures (i.e., the temperature of a blackbody with the same radiance.) For unapodized spectra, brightness temperature is a meaningless concept due to the distortion caused by negative side-lobes that can produce negative-channel radiances.

Barnet et al. (2000) show that a Hamming apodization function is optimal for minimizing the side lobes of the interferometric spectrum response function, while keeping the FWHM as narrow as possible. This spectral response function for the Hamming apodized interferogram is shown as the blue curve in Figure 12. Figure 12 also shows in black the spectral line shape for an AIRS channel at 720.5 cm^{-1}.

The unapodized CrIS spectral response function (red) has a narrow central lobe (0.6/L cm^{-1}, where L is the maximum optical displacement for a band) but side lobes that extend well beyond what is actually shown in the figure . Only 41.2% of the unapodized spectral response function lies within ± 1 FWHM. The width of the central lobe of the Hamming apodized spectral response function (0.9/L cm^{-1}) is 50% larger than that of the unapodized spectral response function. CrIS spectral sampling (0.5/L cm^{-1}) is slightly larger than 1/2 of the Hamming apodized FWHM. The AIRS spectral response function at this frequency (it is narrower at lower frequencies and broader at higher frequencies) is roughly half the width of the Hamming apodized CrIS response function. 95% of the AIRS spectral response function lies within ± 1 FWHM, which is similar to the analogous statistic for the Hamming apodized CrIS. AIRS is sampled at two points per half width, or roughly twice the spectral density of CrIS. The information content of an unapodized spectrum and Hamming apodized spectrum is identical provided all channels in the band are used (Barnet et al., 2000). Because the Hamming

apodized function is highly localized, 0.9/L is a better indication of the effective spectral resolution of an interferometer than is 0.6/L.

Figure 13 shows a sample spectrum observed by AIRS and CrIS. The spectral coverage of AIRS and CrIS is roughly the same. CrIS has 3 bands with the number of channels in each band indicated in the figure, with the sampling, $\Delta\nu$, of each band also indicated on the figure. AIRS is comprised of a number of mini-arrays of detectors with the number of channels in each array indicated. Some very small gaps exist between some of the arrays, as indicated in the AIRS figure. Spectral intervals covered by CrIS that are outside the AIRS spectral coverage are also indicated. In addition, AIRS has some "dead" channels, whose radiances are not included in the AIRS spectrum, but whose locations are not indicated by gaps in the black bars. Figure 14 shows a blow up of this spectrum from 650 cm^{-1} to 780 cm^{-1}. It is apparent that the spectral lines of the CO_2 absorption band in this spectral region are much better resolved by AIRS than by CrIS.

CrIS is comprised of three bands, with L = 0.8 cm^{-1}, 0.4 cm^{-1}, and 0.2 cm^{-1}. The spectral intervals of these bands are shown by the black bars in the lower panel of Figure 13, as well as the number of channels in each band. The effective spectral resolution of CrIS, as well as the spectral sampling, is roughly a factor of 2 larger (poorer) than of AIRS in all bands. In band 2, there is little difference in the appearance of spectra of AIRS and CrIS because the water vapor lines are well resolved even with the poorer spectral resolution of CrIS. In band 3, there is also little difference, because neither spectral resolution is sufficient to resolve the lines.

Simulation studies have shown that products of similar accuracy can be obtained from both AIRS and CrIS, even with the poorer spectral resolution of CrIS. This is because CrIS is expected to have better signal to noise than AIRS. Figure 15 shows the AIRS flight model channel noise as well as the noise predicted for Hamming apodized CrIS channels (given by 0.6 times the unapodized CrIS channel noise). Figure 15 shows that CrIS is expected to have considerably less noise than AIRS. It is the lower noise of CrIS compared to AIRS that compensates for its poorer spectral resolution and spectral sampling, as compared to AIRS, and allows it to achieve soundings of similar accuracy performance compared to AIRS.

References

Barnet CD., Blaisdell JM, Susskind J (2000) Practical methods for rapid and accurate computation of interferometric spectra for remote sensing applications. IEEE Trans Geosci Remote Sensing 38:169-183.

Brigham EO (1988) The fast fourier transform and its applications. Englewood Cliffs, Prentice-Hall NJ.

Goldberg MD, Qu Y, McMillin LM, Wolff W, Zhou L, Divarkla M (2003) AIRS near-real-time products and algorithms in support of operational numerical weather prediction. IEEE Trans Geosci Remote Sensing 41:379-389.

Kaplan, LD, Chahine MT, Susskind J, Searl, JE (1977) Spectral band passes for a high precision satellite sounder. Appl Opt 16:322-325.

Lin, SJ, Atlas R, Yeh KS (2004) Global weather prediction and high end computing at NASA. Computing in Science and Engineering:29-35.

Mehta, A, Susskind J (1999) Outgoing longwave radiation from the TOVS Pathfinder Path A data set. J Geophys Res 104:12193-12212.

Pagano, TS, Aumann HH, Hagan DE, Overoye K (2003) Prelaunch and in-flight radiometric calibration of the Atmospheric Infrared Sounder (AIRS). IEEE Trans Geosci Remote Sensing 41:265-273.

Rosenkranz, PW (2000) Retrieval of temperature and moisture profiles from AMSU-A and AMSU-B measurements. In Proc IGARSS.

Susskind, J, Barnet CD, Blaisdell JM (2003) Retrieval of Atmospheric and Surface Parameters from AIRS/AMSU/HSB Data in the Presence of Clouds. IEEE Trans Geosc. Remote Sensing 41:390-409.

Figure Captions

Figure 1. Simulated AIRS noise free spectrum. Gaps in the spectrum indicate planned spectral gaps for AIRS or dead detectors. The colored symbols show channels used for different purposes in the physical retrieval of geophysical parameters.

Figure 2. Temperature weighting functions for sample AIRS like channels and AMSU A channels.

Figure 3. The number of cases for which a given cloud fraction was retrieved (black) and the percentage of those cases in which a successful retrieval was performed (blue). The average effective cloud fraction for all cases and accepted cases is also indicated.

Figure 4. The RMS differences from ECMWF in 1 km layer mean temperatures for accepted cases as a function of retrieved effective cloud fraction.

Figure 5 a. RMS layer mean temperature differences from "truth" for all accepted cases and cases identified as essentially clear in both simulation and real data. b. RMS percent differences from ECMWF in 1 km layer precipitable water for the same cases shown in Figure 5a.

Figure 6 a. RMS layer mean temperature differences with observed data in radiosonde locations. b. RMS layer precipitable water percent differences in radiosonde locations.

Figure 7. Sample retrieved geophysical parameters for ascending orbits on January 25, 2003. Gray indicates missing data due to orbit gaps (clouds) as well as rejected retrievals (other fields).

Figure 8. Comparison of AIRS retrieved temperatures and those predicted from the ECMWF three hour forecast.

Figure 9. Sea level pressure forecast anomaly correlation coefficients with the NCEP analysis averaged over 13 forecasts using AIRS temperature soundings (red) and not using AIRS temperature soundings (black). Higher anomaly correlation coefficients indicate improved forecast skill.

Figure 10. Global extratropical cyclone position and intensity RMS errors from 11 5 day forecasts using differing amounts of AIRS temperature soundings.

Figure 11. 72 hour forecast of sea level pressure in the vicinity of tropical storm Beni based on forecasts with and without the benefit of AIRS temperature soundings, as well as the verifying analysis.

Figure 12. Channel response functions at 720.5 cm^{-1} for AIRS (black), CrIS without apodization (red), and CrIS with Hamming apodization (blue).

Figure 13. Simulated AIRS and CrIS Hamming apodized spectra for a sample scene. Gaps in AIRS spectral coverage relative to CrIS are indicated in the figure.

Figure 14. Comparison of AIRS and CrIS spectra between 650 cm^{-1} and 780 cm^{-1}.

Figure 15. AIRS flight model noise and predicted CrIS Hamming apodized noise.

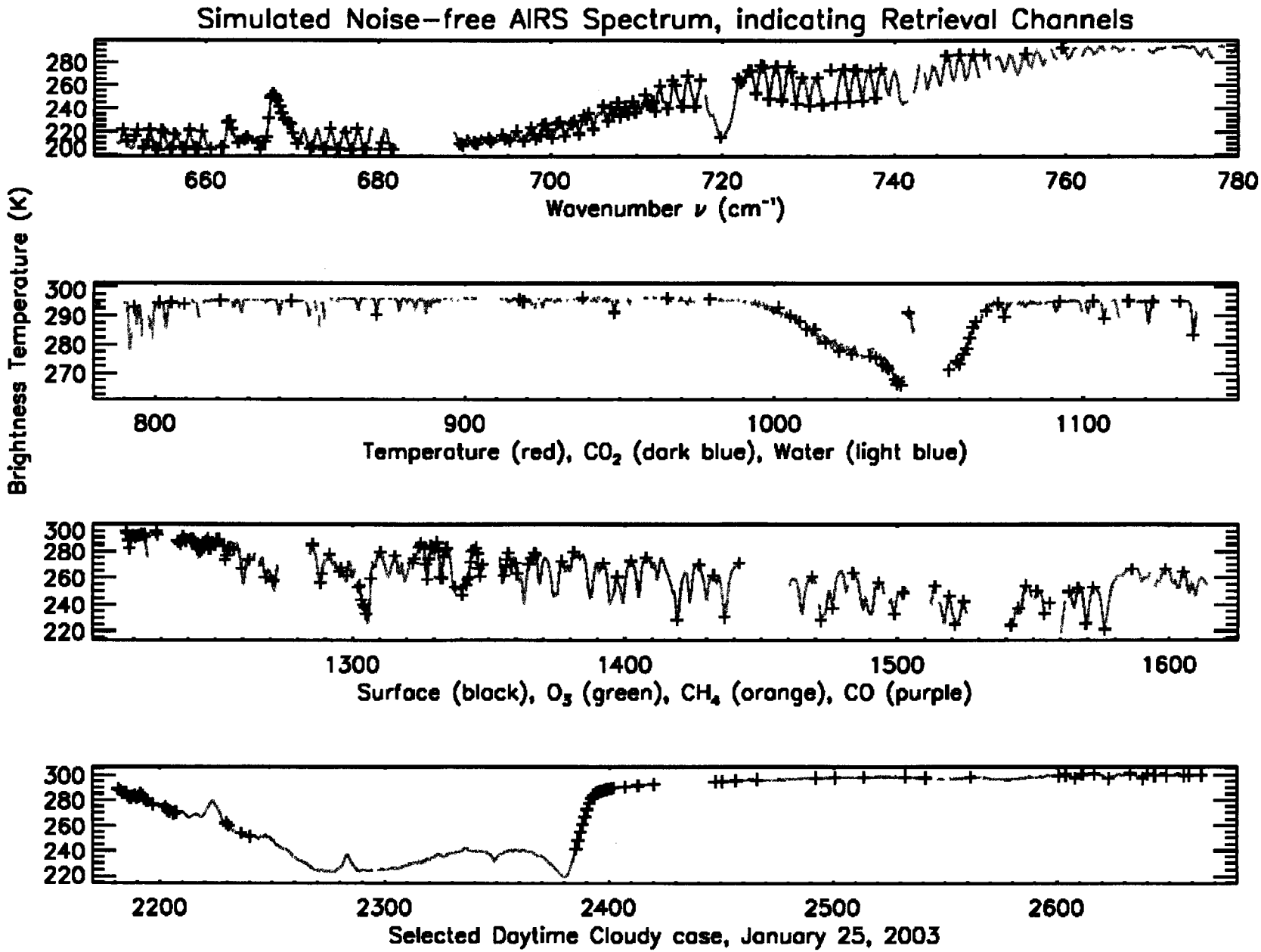
Simulated Noise–free AIRS Spectrum, indicating Retrieval Channels
Brightness Temperature (K)
280
260
240
220
200
660
680
700
720
740
760
780
Wavenumber ν (cm⁻¹)
300
290
280
270
800
900
1000
1100
Temperature (red), CO2 (dark blue), Water (light blue)
300
280
260
240
220
1300
1400
1500
1600
Surface (black), O3 (green), CH4 (orange), CO (purple)
300
280
260
240
220
2200
2300
2400
2500
2600
Selected Daytime Cloudy case, January 25, 2003

Figure 1

TEMPERATURE WEIGHTING FUNCTIONS

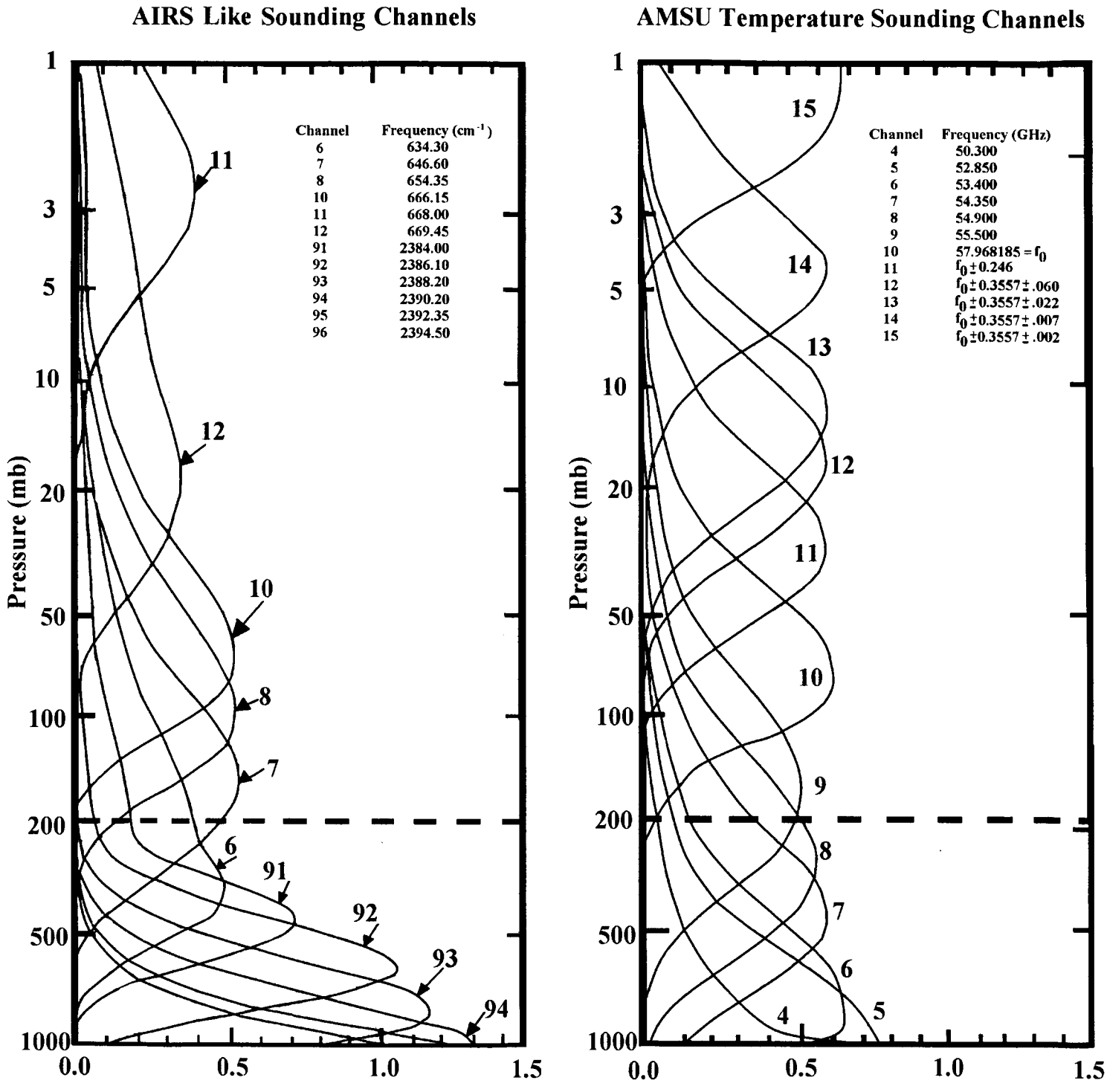

Figure 2

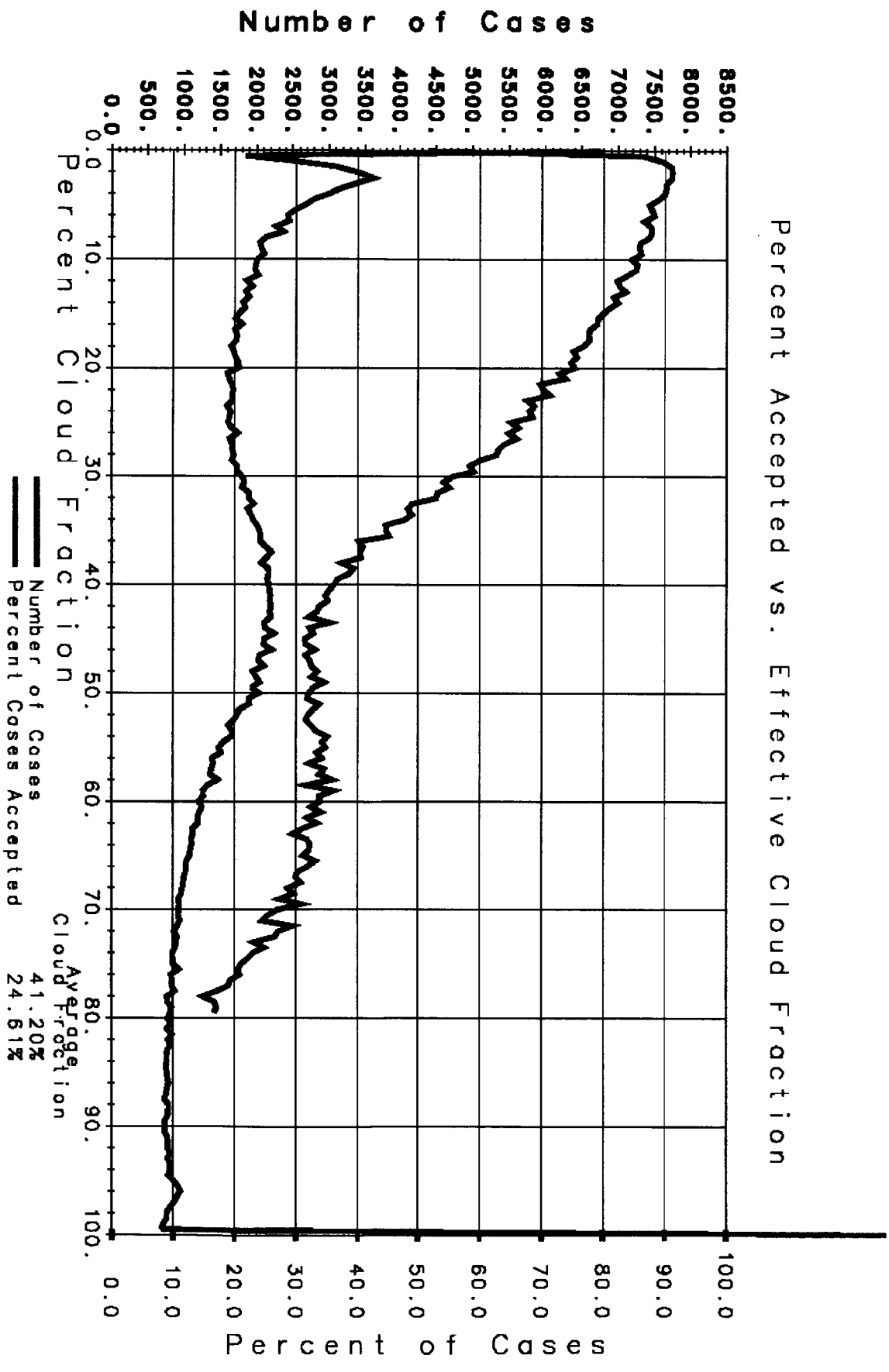
Number of Cases
8500.
8000.
7500.
7000.
6500.
6000.
5500.
5000.
4500.
4000.
3500.
3000.
2500.
2000.
1500.
1000.
500.
0.0
0.0
10.
20.
30.
40.
50.
60.
70.
80.
90.
100.
Percent Cloud Fraction
Number of Cases
Percent Cases Accepted
Average Cloud Fraction
41.20%
24.61%
Percent Accepted vs. Effective Cloud Fraction
100.0
90.0
80.0
70.0
60.0
50.0
40.0
30.0
20.0
10.0
0.0
Percent of Cases

Figure 3

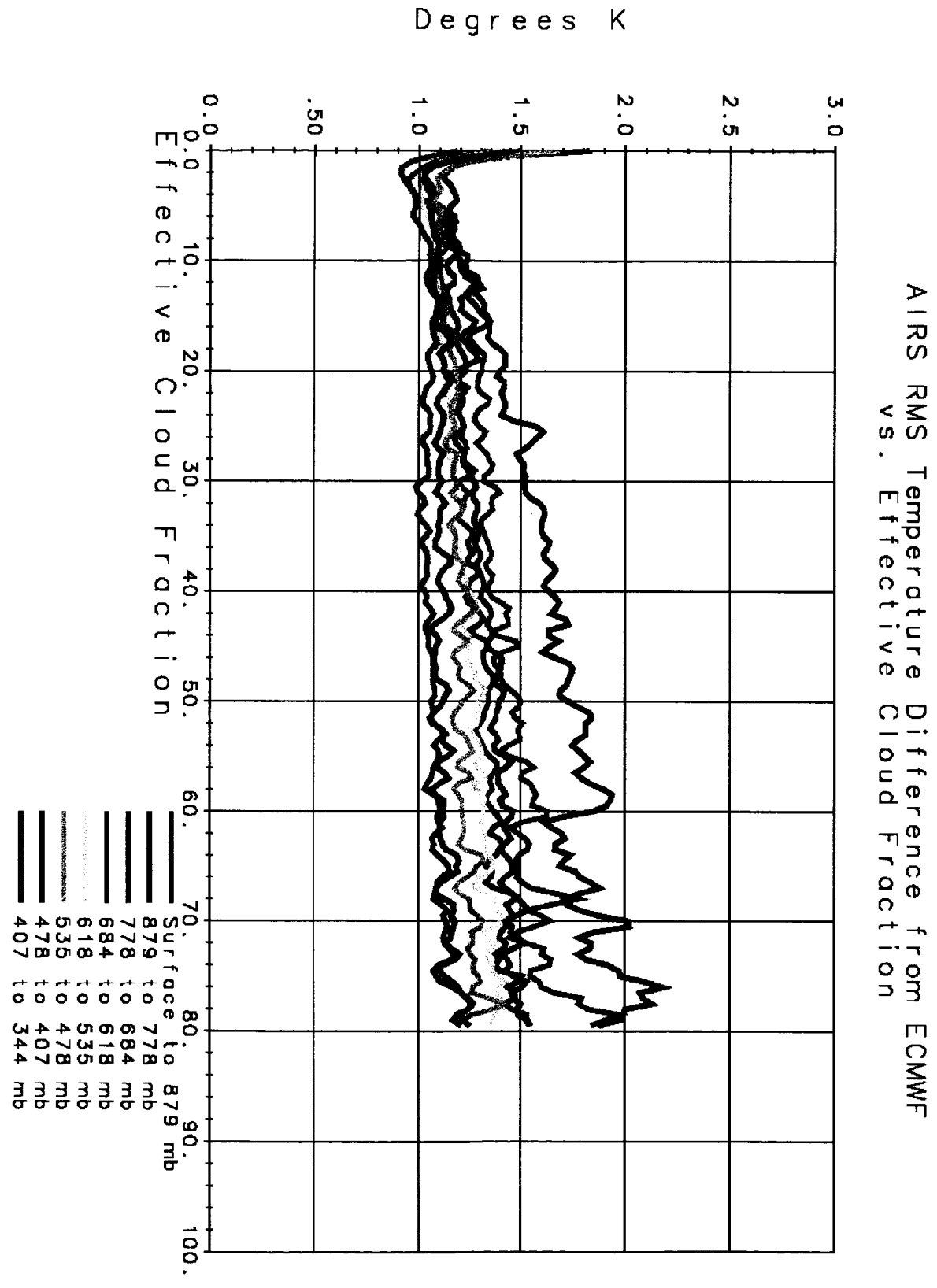
AIRS RMS Temperature Difference from ECMWF
vs. Effective Cloud Fraction
Degrees K
0.0
.50
1.0
1.5
2.0
2.5
3.0
Effective Cloud Fraction
0.0
10.
20.
30.
40.
50.
60.
70.
80.
90.
100.
Surface to 879 mb
879 to 778 mb
778 to 684 mb
684 to 618 mb
618 to 535 mb
535 to 478 mb
478 to 407 mb
407 to 344 mb

Figure 4

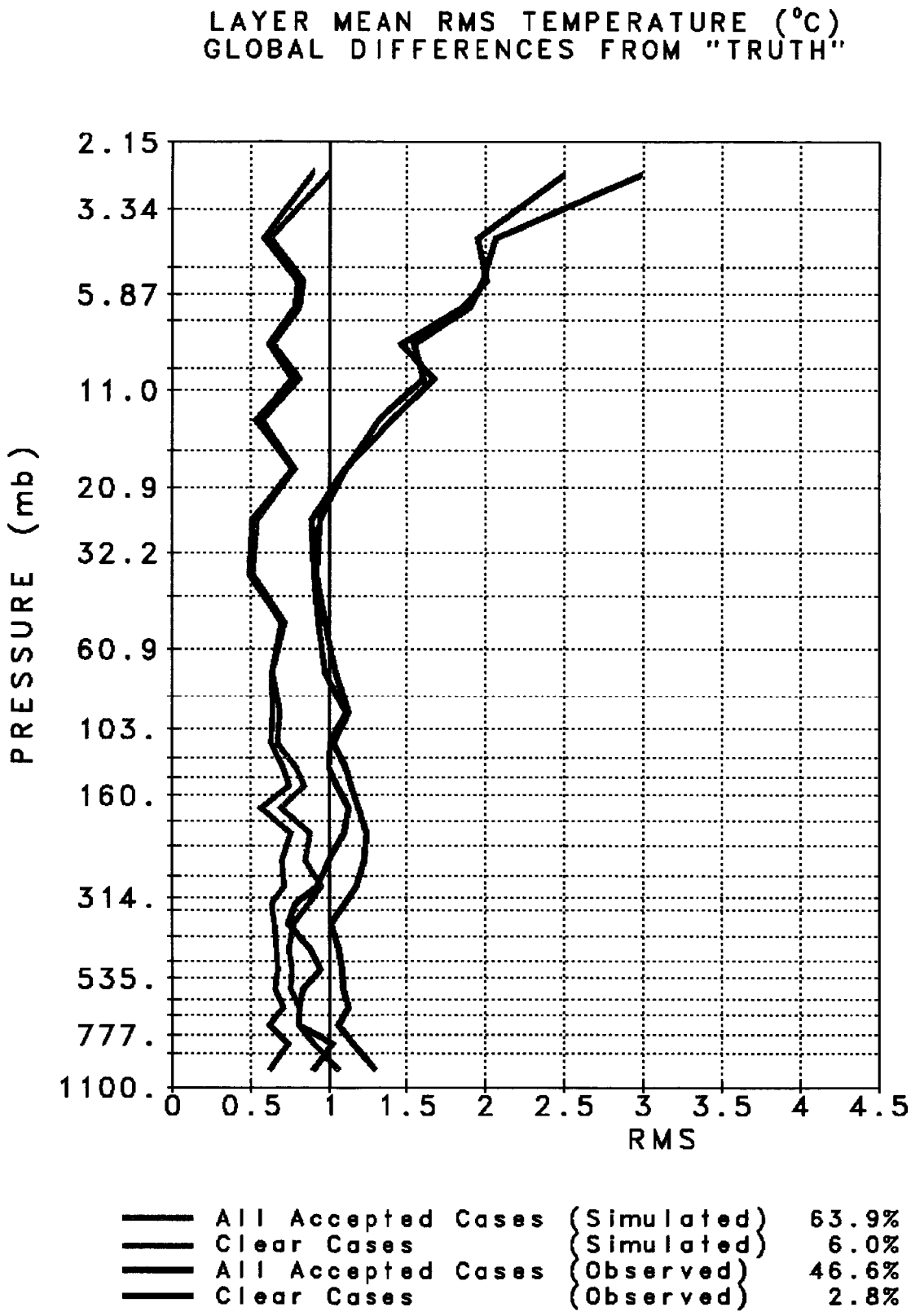
LAYER MEAN RMS TEMPERATURE (°C)
GLOBAL DIFFERENCES FROM "TRUTH"
PRESSURE (mb)
2.15
3.34
5.87
11.0
20.9
32.2
60.9
103.
160.
314.
535.
777.
1100.
0
0.5
1
1.5
2
2.5
3
3.5
4
4.5
RMS
All Accepted Cases (Simulated) 63.9%
Clear Cases (Simulated) 6.0%
All Accepted Cases (Observed) 46.6%
Clear Cases (Observed) 2.8%

Figure 5a

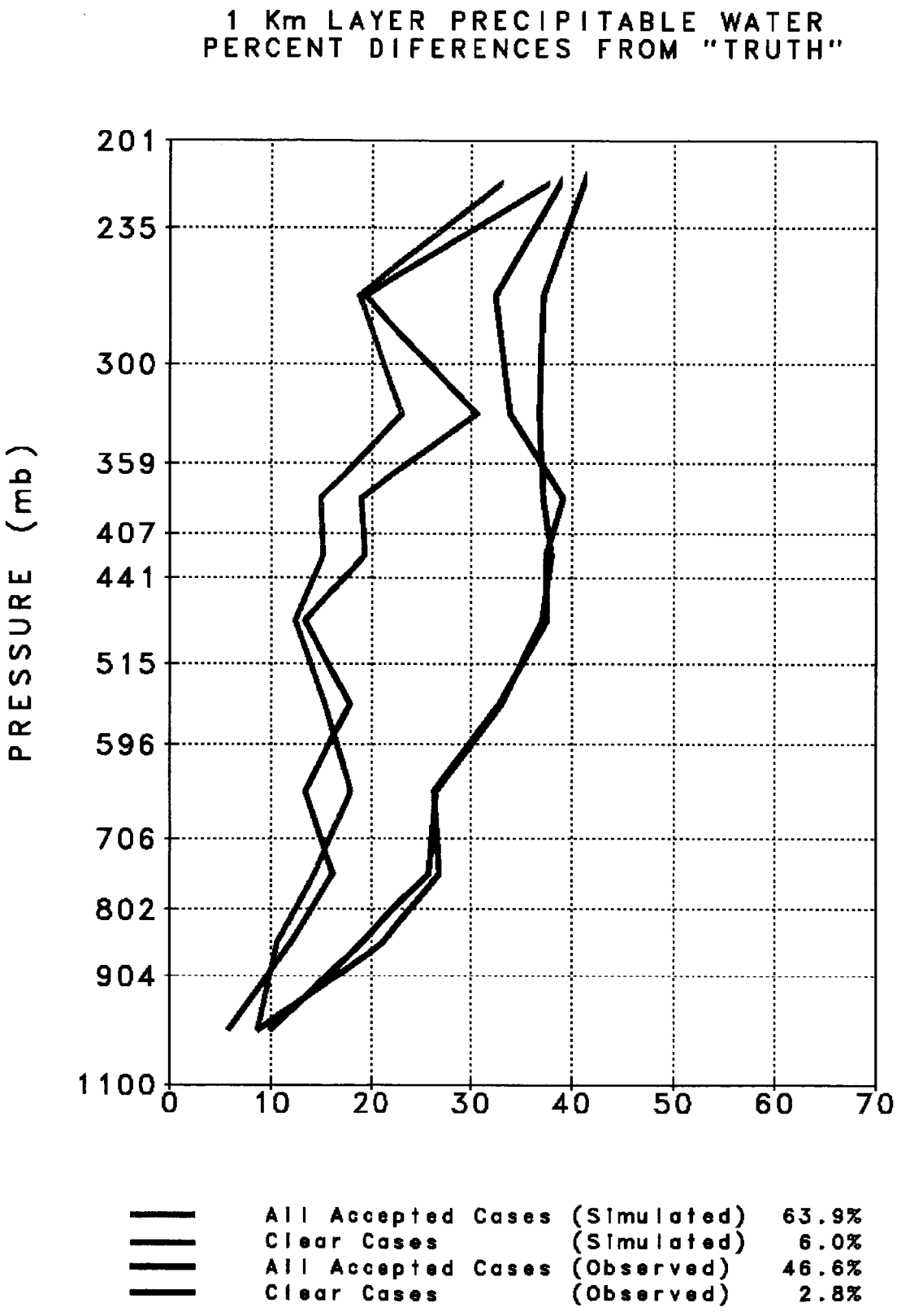
1 Km LAYER PRECIPITABLE WATER
PERCENT DIFERENCES FROM "TRUTH"
PRESSURE (mb)
201
235
300
359
407
441
515
596
706
802
904
1100
0
10
20
30
40
50
60
70
All Accepted Cases (Simulated) 63.9%
Clear Cases (Simulated) 6.0%
All Accepted Cases (Observed) 46.6%
Clear Cases (Observed) 2.8%

Figure 5b

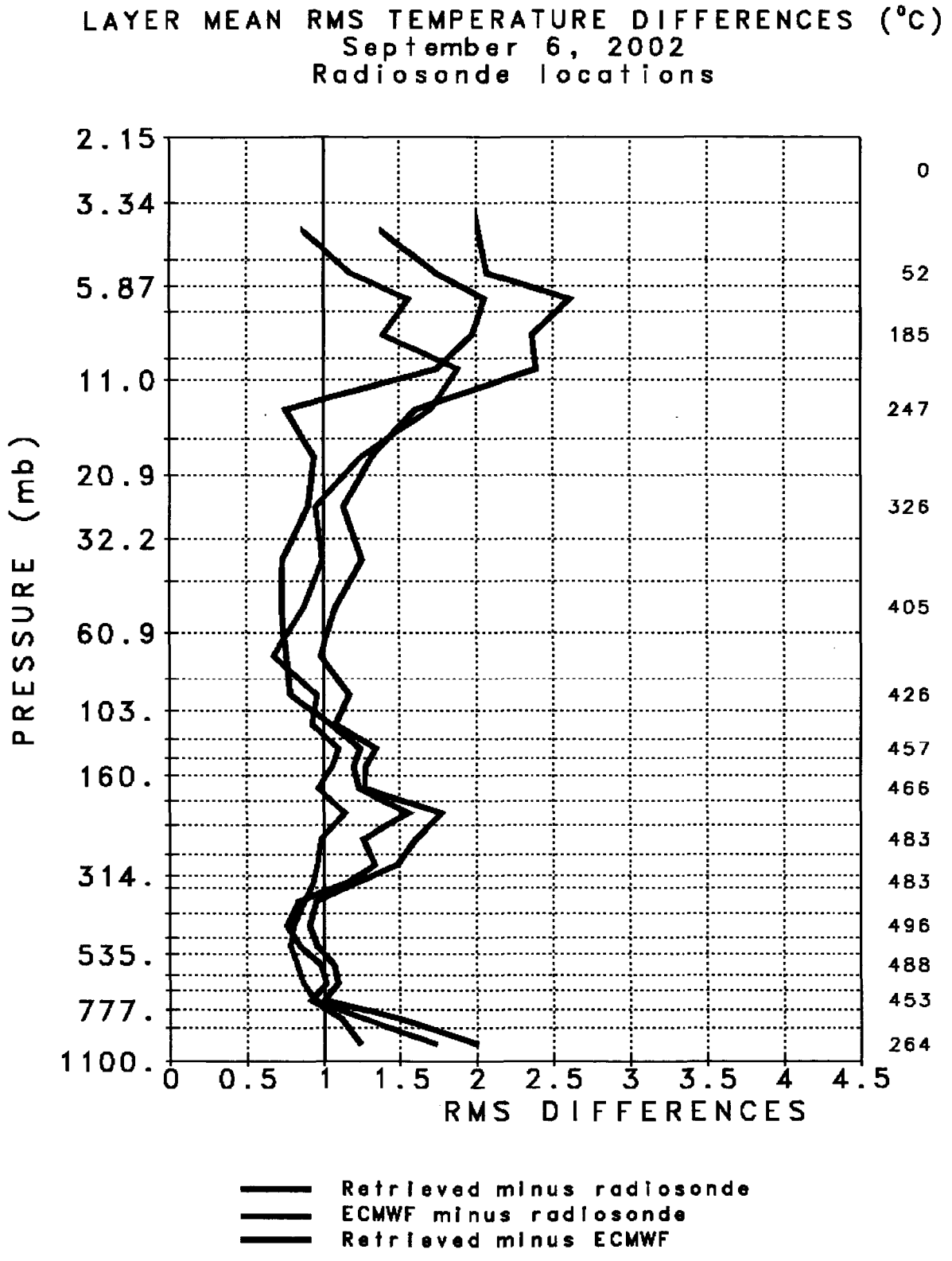
LAYER MEAN RMS TEMPERATURE DIFFERENCES (°C)
September 6, 2002
Radiosonde locations
PRESSURE (mb)
2.15
3.34
5.87
11.0
20.9
32.2
60.9
103.
160.
314.
535.
777.
1100.
0
52
185
247
326
405
426
457
466
483
483
496
488
453
264
0 0.5 1 1.5 2 2.5 3 3.5 4 4.5
RMS DIFFERENCES
Retrieved minus radiosonde
ECMWF minus radiosonde
Retrieved minus ECMWF

Figure 6a

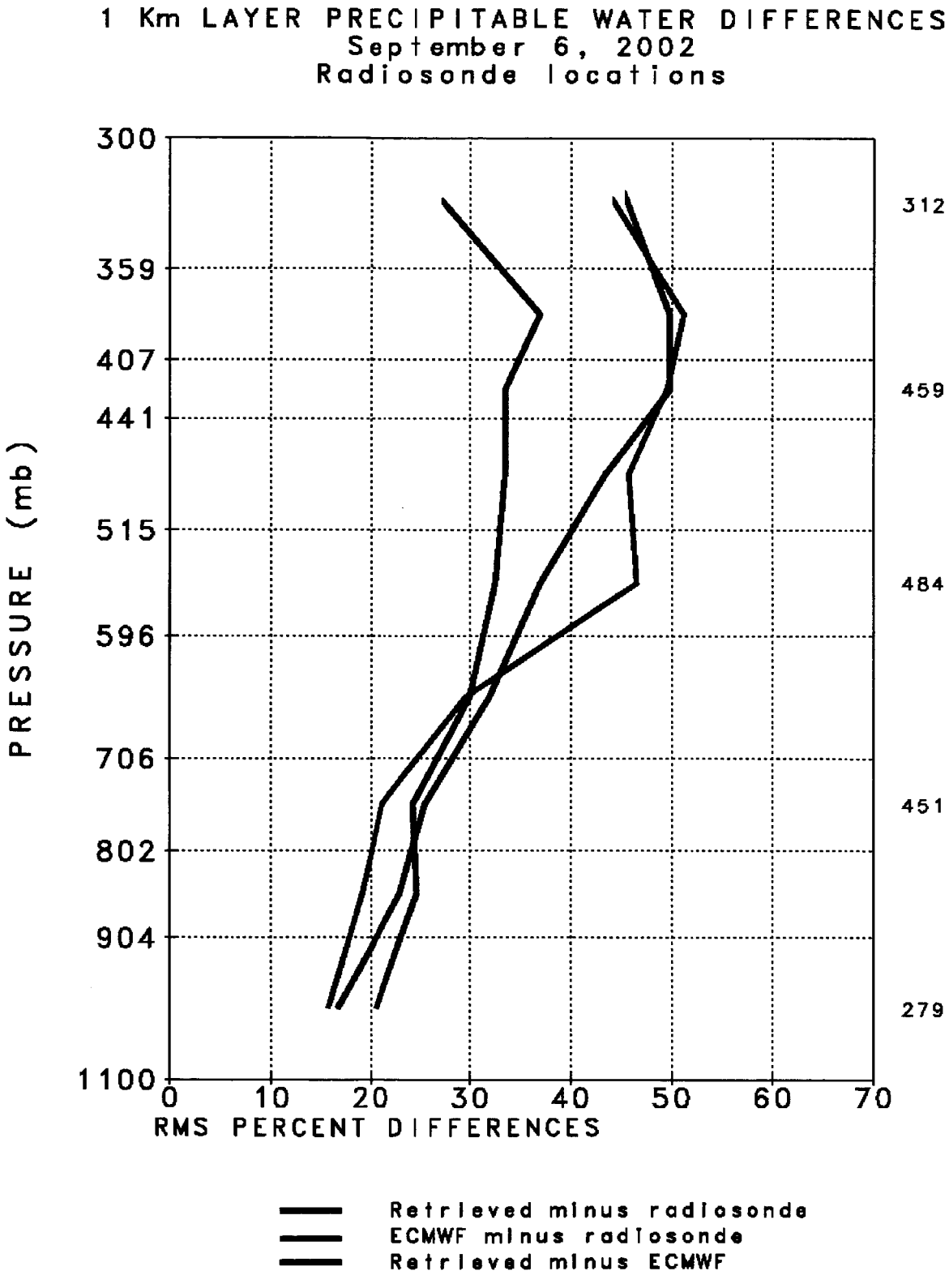
1 Km LAYER PRECIPITABLE WATER DIFFERENCES
September 6, 2002
Radiosonde locations
PRESSURE (mb)
300
359
407
441
515
596
706
802
904
1100
312
459
484
451
279
0
10
20
30
40
50
60
70
RMS PERCENT DIFFERENCES
Retrieved minus radiosonde
ECMWF minus radiosonde
Retrieved minus ECMWF

Figure 6b

S
ing Channels
Frequency (GHz)
50.300
52.850
53.400
54.350
54.900
55.500
57.968185 = f_0
$f_0 \pm 0.246$
$f_0 \pm 0.3557 \pm .060$
$f_0 \pm 0.3557 \pm .022$
$f_0 \pm 0.3557 \pm .007$
$f_0 \pm 0.3557 \pm .002$
1.0
1.5

(a)
AIRS 700 mb Temperature (K)
January 29, 2003
(b) January 29, 2003 ECMWF 700 mb Temperature (K) Collocated to AIRS
(c)
700 AIRS minus ECMWF (K)
GLOBAL MEAN= 272.43 STANDARD DEV= 11.17
(d)
100 AIRS minus ECMWF (K)
GLOBAL MEAN= 272.35 STANDARD DEV= 11.21
226.0 236.0 246.0 256.0 266.0 276.0 286.0 296.0 306.0
80 N
60 N
30 N
EQ
30 S
60 S
90 S
180
120 W
60 W
0
60 E
120 E
180

Figure 8

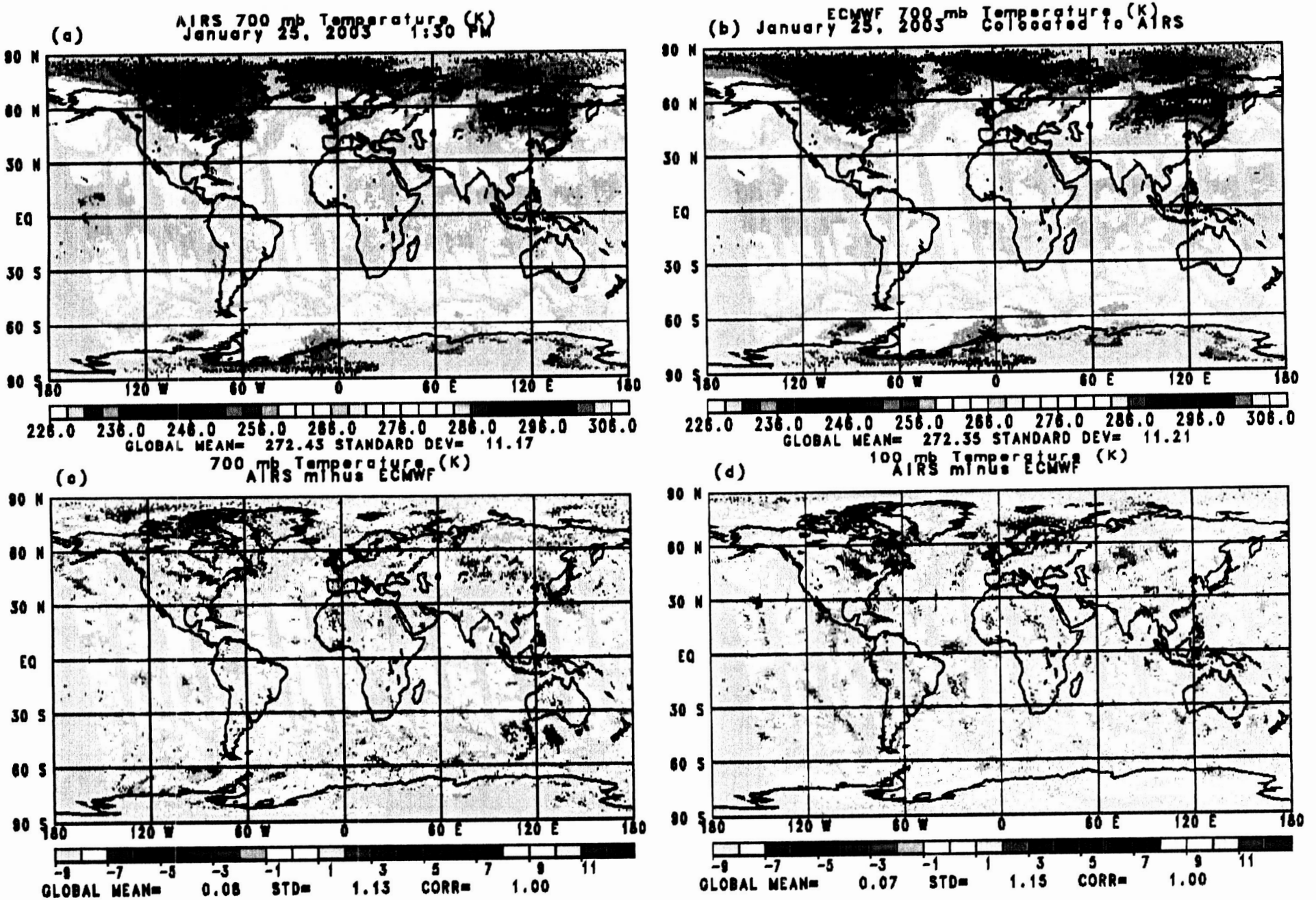
(a)
AIRS 700 mb Temperature (K)
January 25, 2003 1:30 PM
90 N
60 N
30 N
EQ
30 S
60 S
90 S
180
120 W
60 W
0
60 E
120 E
180
226.0 236.0 246.0 256.0 266.0 276.0 286.0 296.0 306.0
GLOBAL MEAN= 272.43 STANDARD DEV= 11.17
(b) January 25, 2003
ECMWF 700 mb Temperature (K)
Collocated to AIRS
226.0 236.0 246.0 256.0 266.0 276.0 286.0 296.0 306.0
GLOBAL MEAN= 272.35 STANDARD DEV= 11.21
(c)
700 mb Temperature (K)
AIRS minus ECMWF
-9 -7 -5 -3 -1 1 3 5 7 9 11
GLOBAL MEAN= 0.08 STD= 1.13 CORR= 1.00
(d)
100 mb Temperature (K)
AIRS minus ECMWF
-9 -7 -5 -3 -1 1 3 5 7 9 11
GLOBAL MEAN= 0.07 STD= 1.15 CORR= 1.00

Figure 8

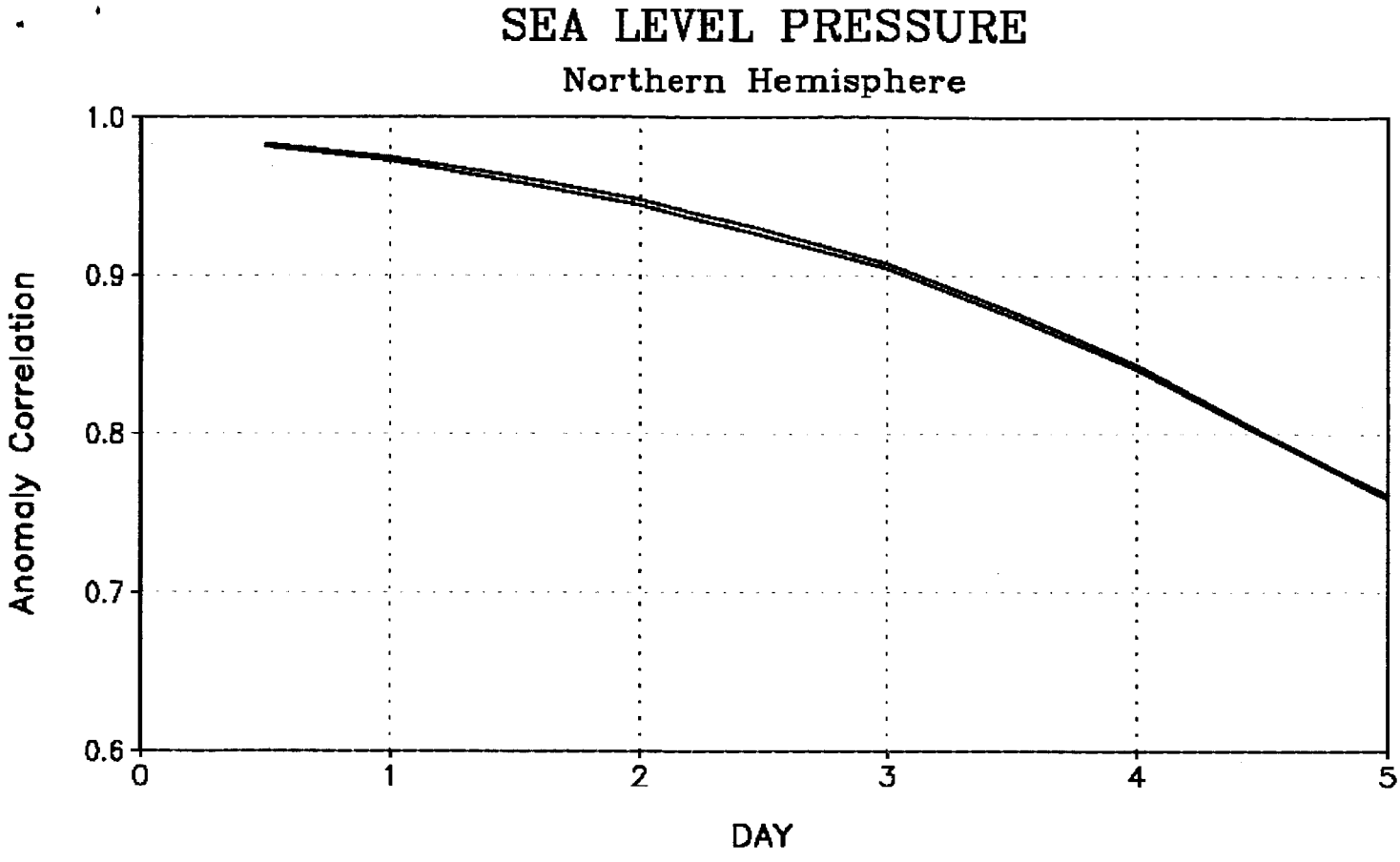
SEA LEVEL PRESSURE
Northern Hemisphere
Anomaly Correlation
1.0
0.9
0.8
0.7
0.6
0
1
2
3
4
5
DAY

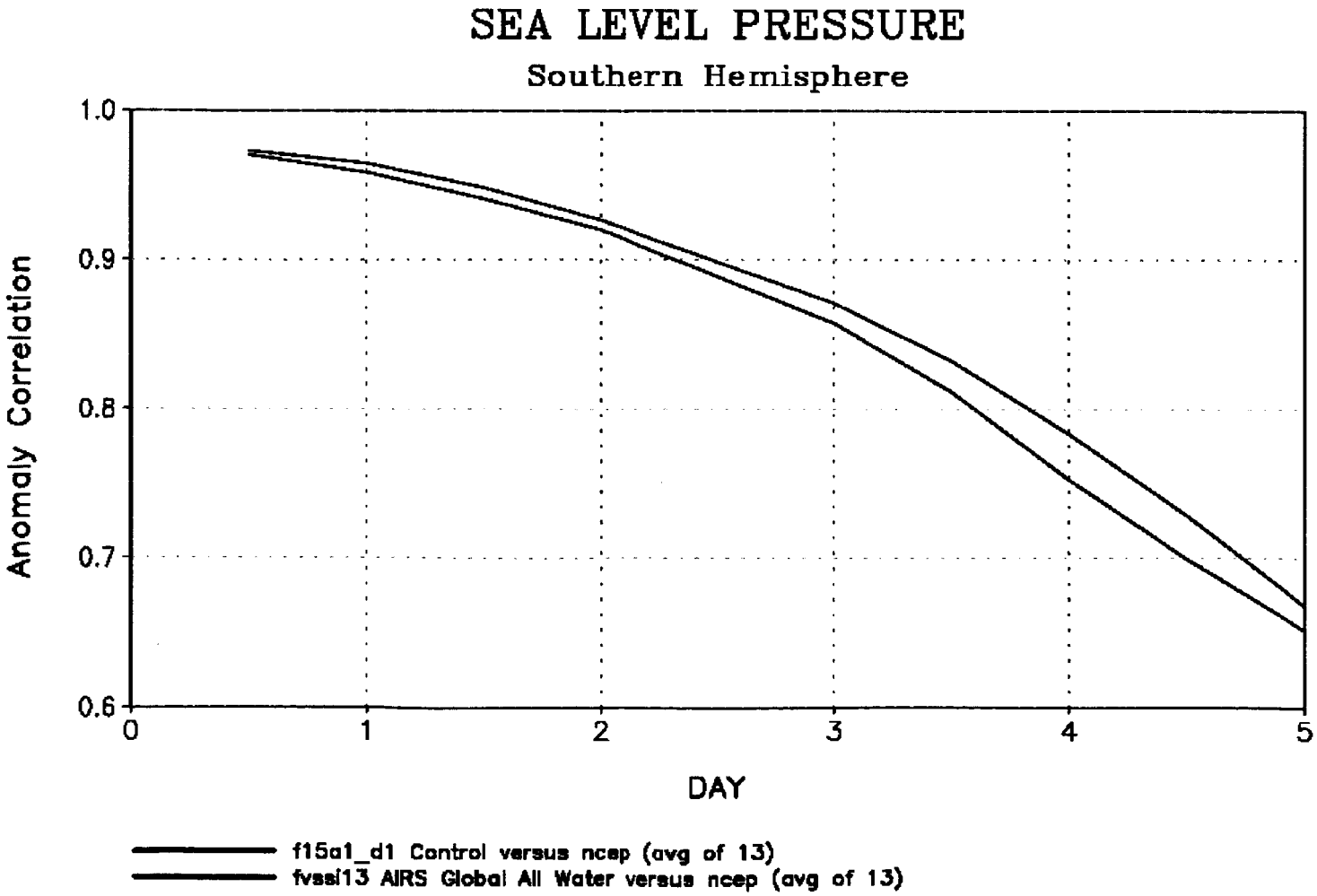
SEA LEVEL PRESSURE
Southern Hemisphere
Anomaly Correlation
1.0
0.9
0.8
0.7
0.6
0
1
2
3
4
5
DAY
f15a1_d1 Control versus ncep (avg of 13)
fvssi13 AIRS Global All Water versus ncep (avg of 13)

Figure 9

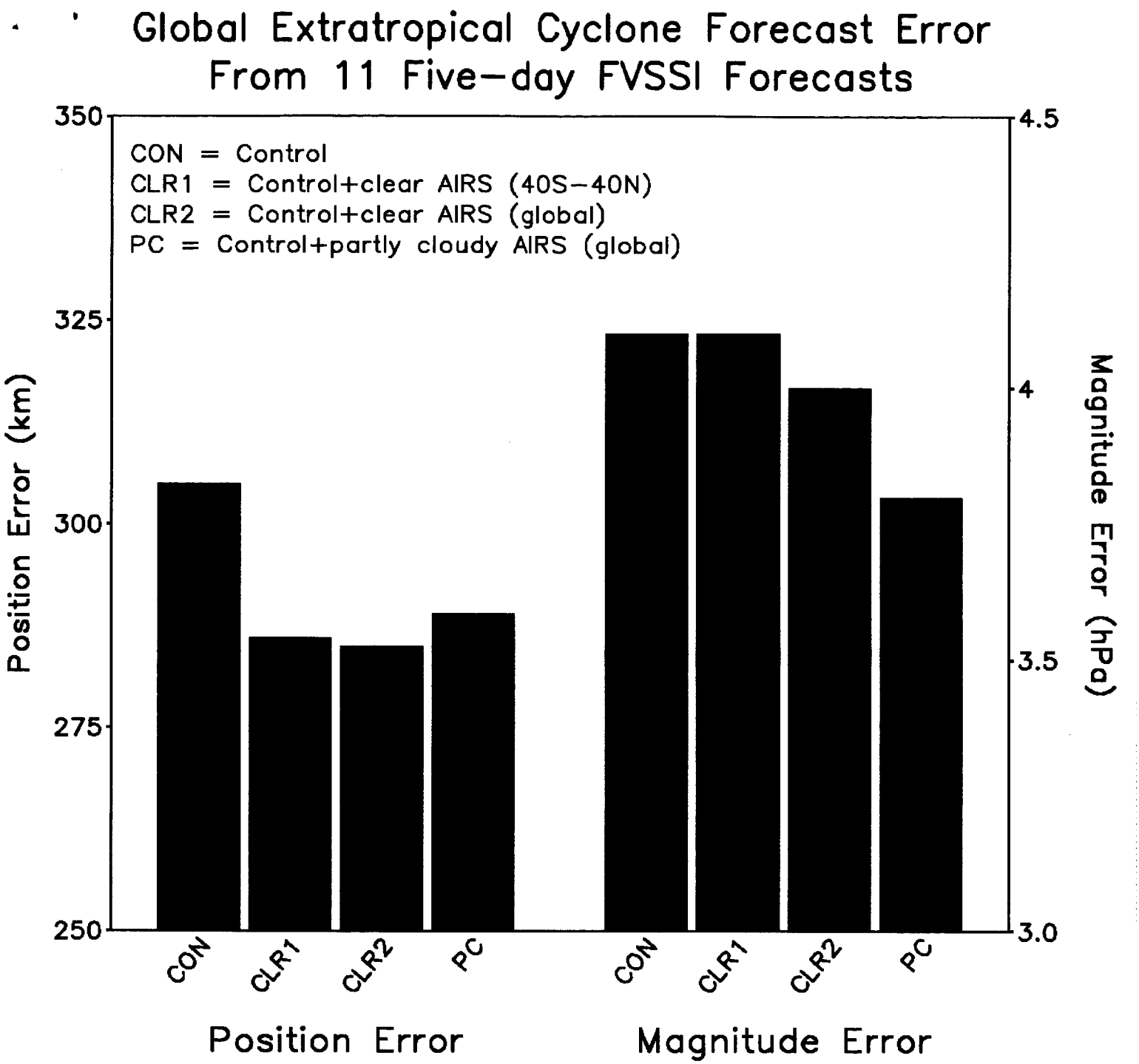
Global Extratropical Cyclone Forecast Error
From 11 Five-day FVSSI Forecasts
CON = Control
CLR1 = Control+clear AIRS (40S-40N)
CLR2 = Control+clear AIRS (global)
PC = Control+partly cloudy AIRS (global)
Position Error (km)
Magnitude Error (hPa)
350
325
300
275
250
4.5
4
3.5
3.0
CON
CLR1
CLR2
PC
CON
CLR1
CLR2
PC
Position Error
Magnitude Error

Figure 10

Impact of AIRS on 72hr Forecast of Sea Level Pressure

Control Forecast

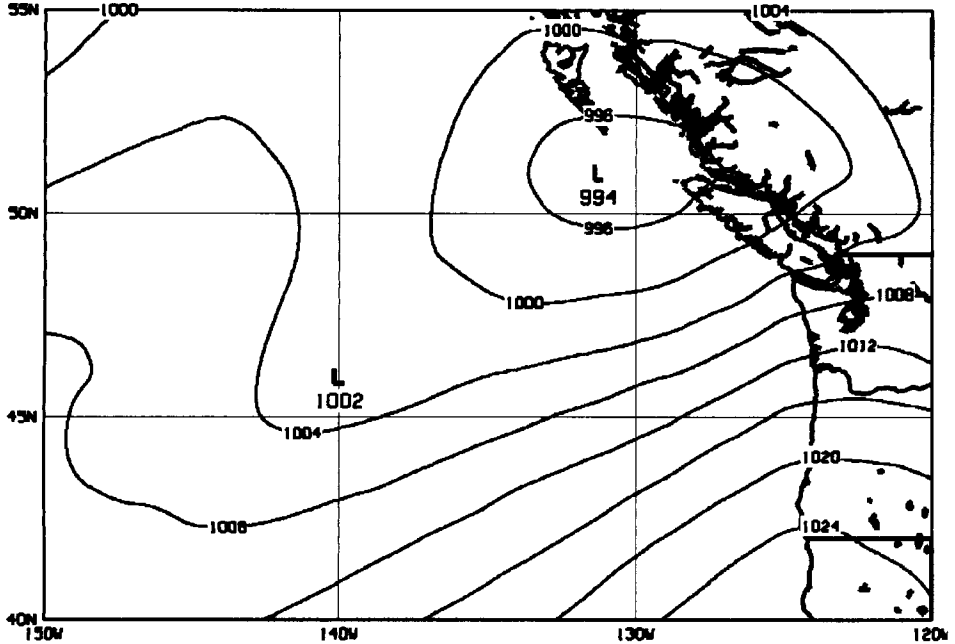

AIRS Forecast

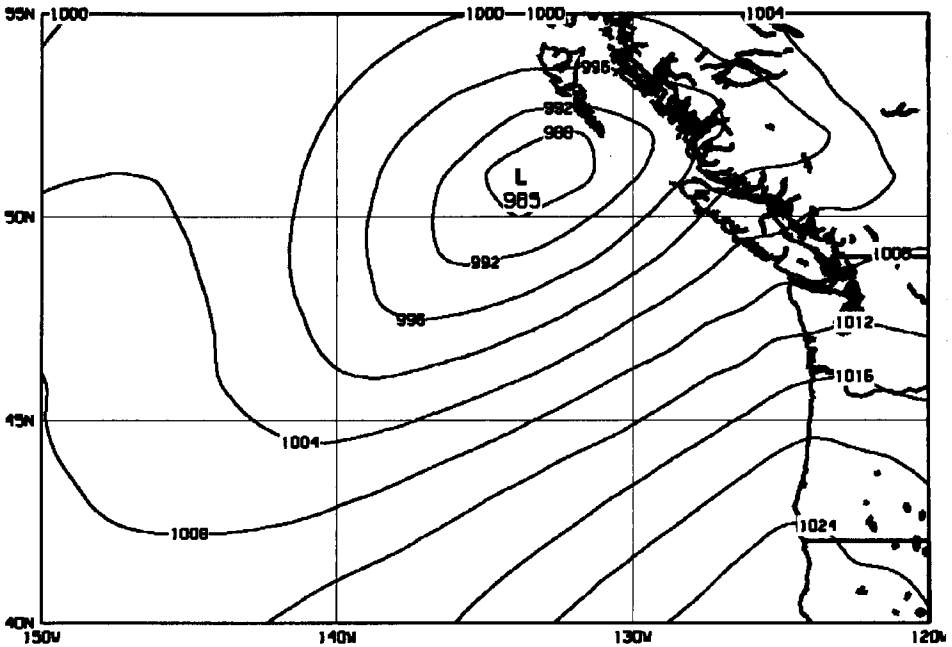

NCEP Analysis

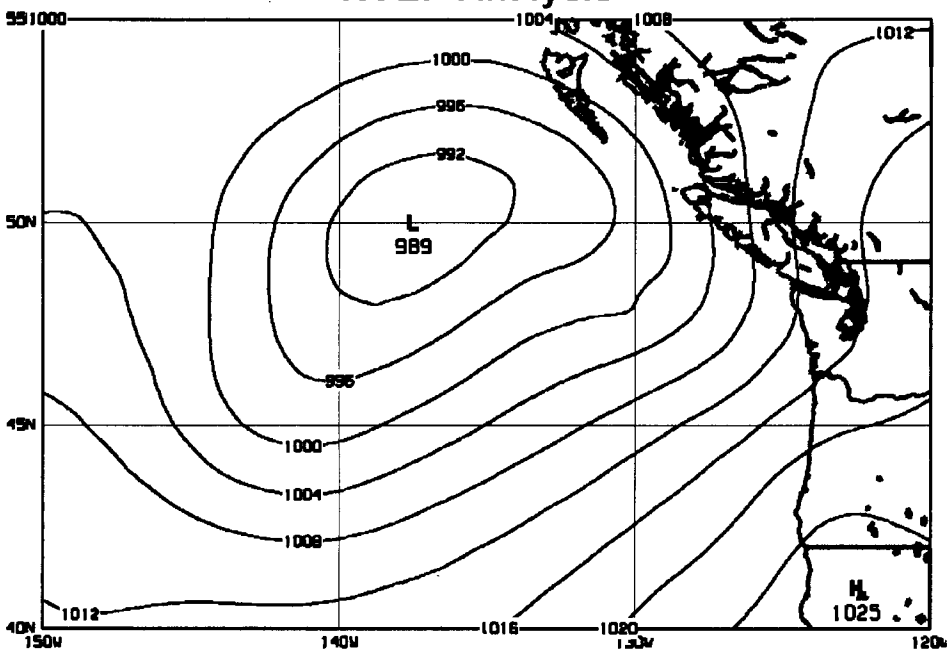

January 31, 2003 00Z

Figure 11

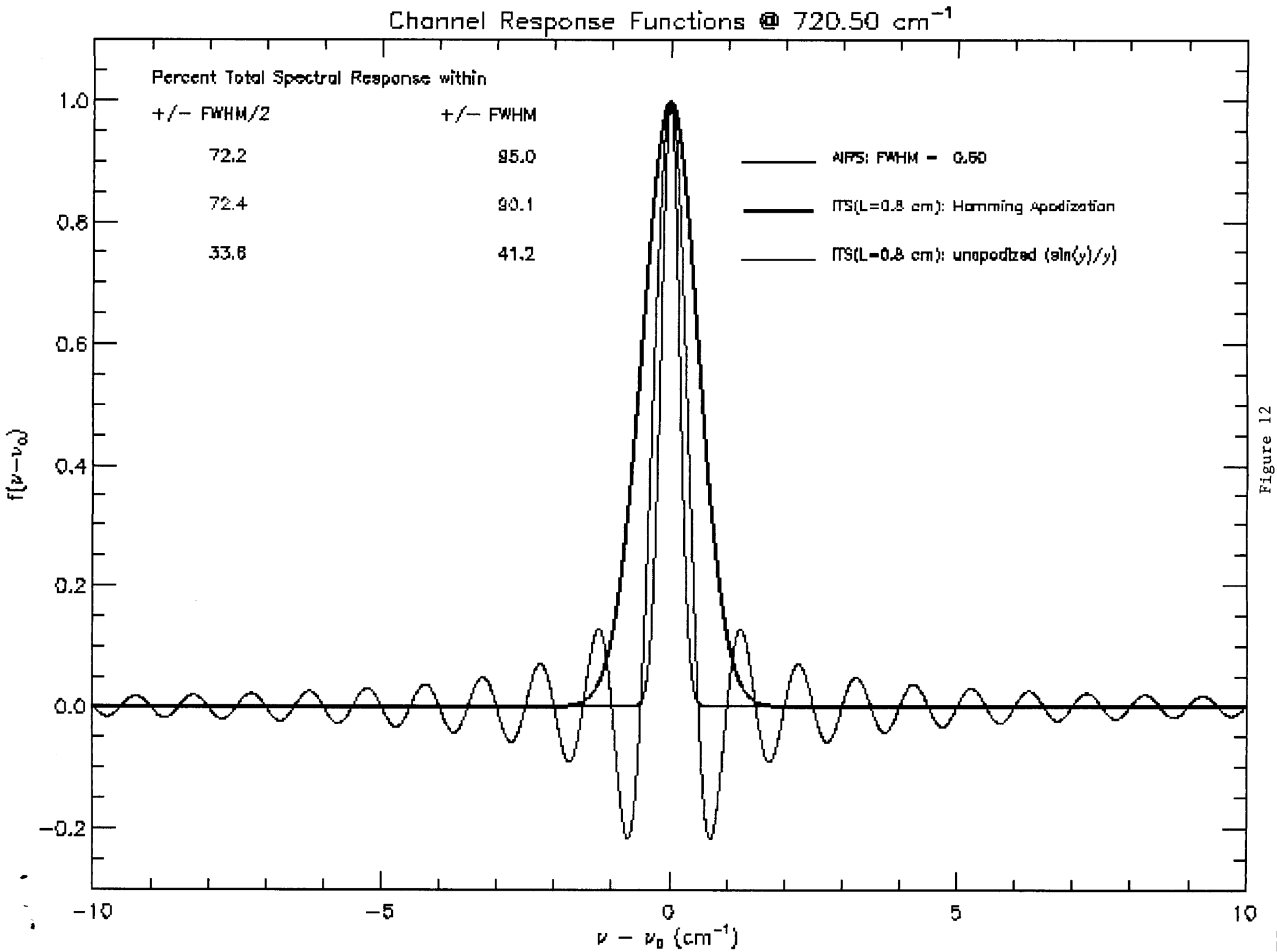
Channel Response Functions @ 720.50 cm^{-1}
Percent Total Spectral Response within
+/− FWHM/2
+/− FWHM
72.2
95.0
72.4
90.1
33.6
41.2
AIRS: FWHM = 0.50
ITS(L=0.8 cm): Hamming Apodization
ITS(L=0.8 cm): unapodized (sin(y)/y)
f(ν−ν0)
1.0
0.8
0.6
0.4
0.2
0.0
−0.2
−10
−5
0
5
10
ν − ν0 (cm^{-1})

Figure 12

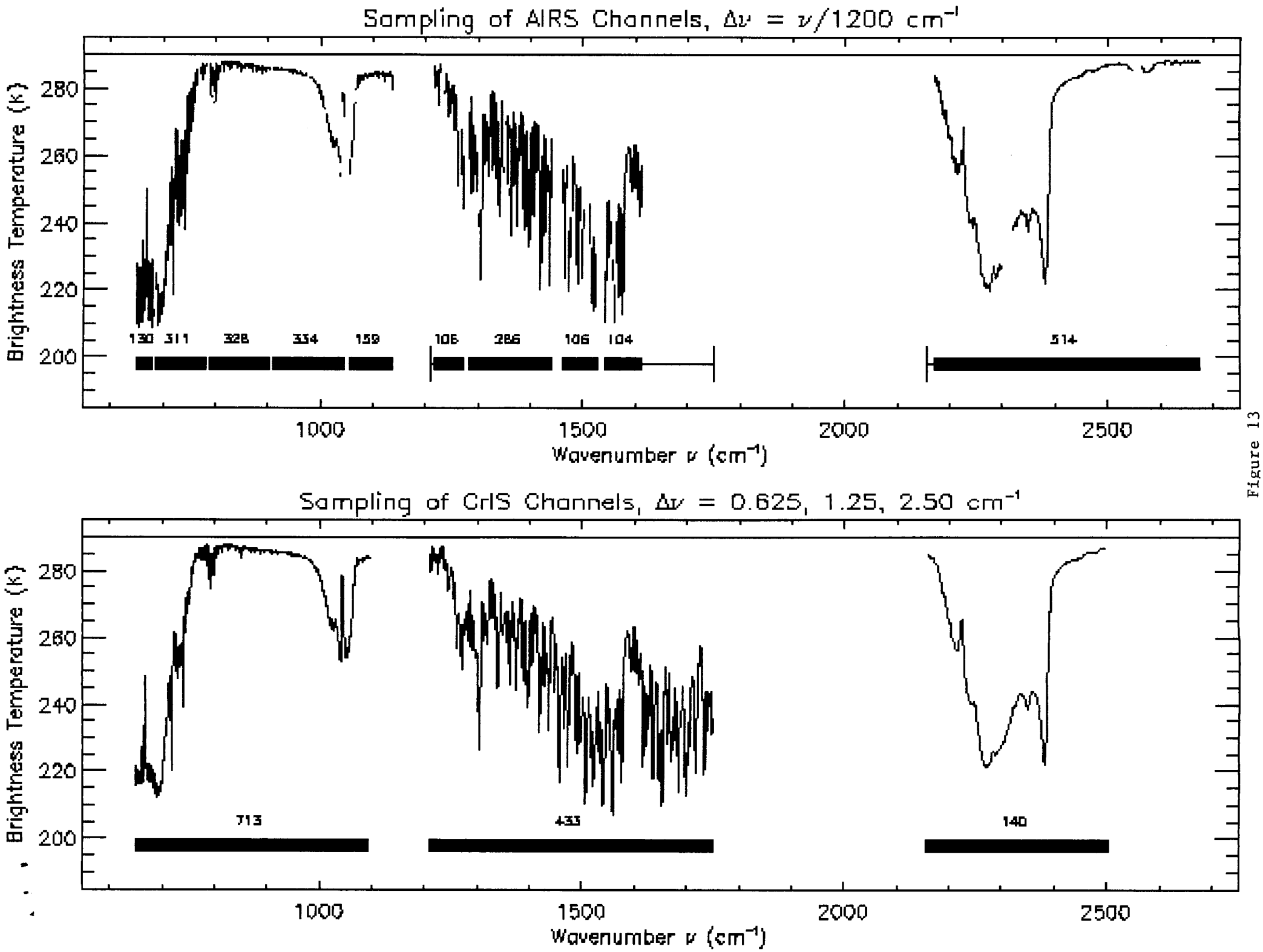
Sampling of AIRS Channels, Δν = ν/1200 cm⁻¹
Brightness Temperature (K)
280
260
240
220
200
130
311
328
334
159
105
286
106
104
514
1000
1500
2000
2500
Wavenumber ν (cm⁻¹)
Sampling of CrIS Channels, Δν = 0.625, 1.25, 2.50 cm⁻¹
Brightness Temperature (K)
280
260
240
220
200
713
433
140
1000
1500
2000
2500
Wavenumber ν (cm⁻¹)

Figure 13

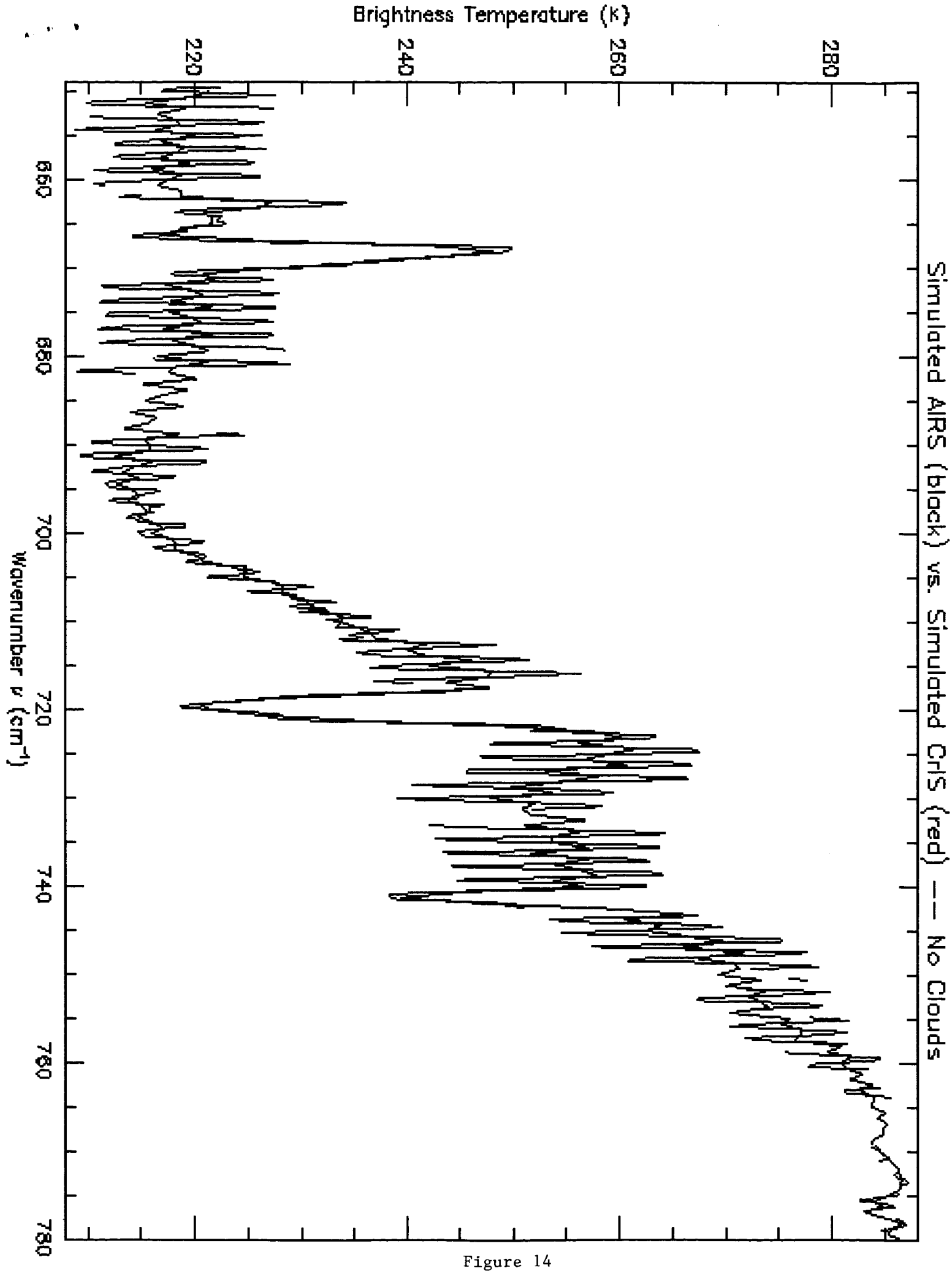
Brightness Temperature (K)
220
240
260
280
660
680
700
720
740
760
780
Wavenumber ν (cm⁻¹)
Simulated AIRS (black) vs. Simulated CrIS (red) — No Clouds

Figure 14

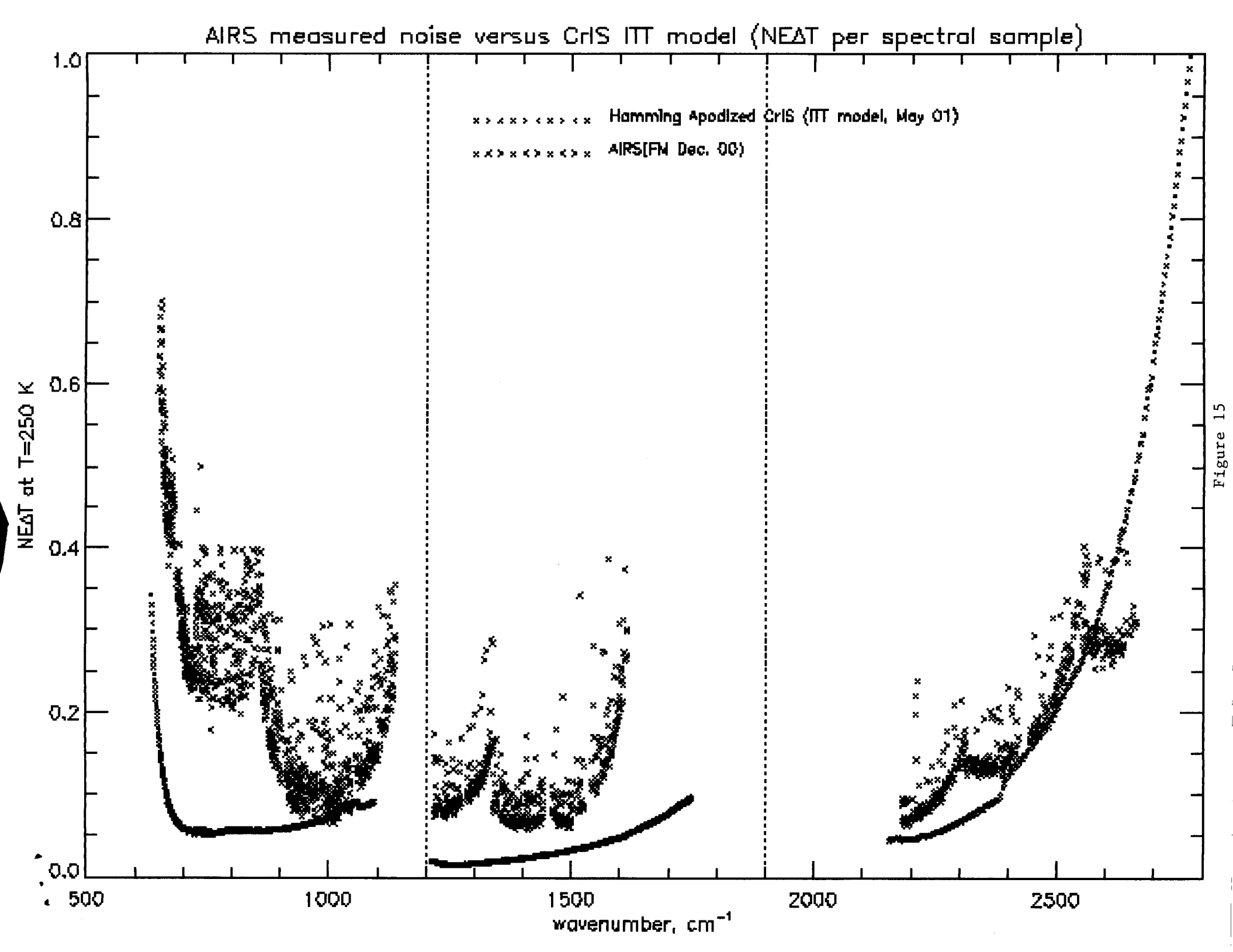
AIRS measured noise versus CrIS ITT model (NEΔT per spectral sample)
Hamming Apodized CrIS (ITT model, May 01)
AIRS(FM Dec. 00)
NEΔT at T=250 K
1.0
0.8
0.6
0.4
0.2
0.0
500
1000
1500
2000
2500
wavenumber, cm-1

Figure 15